Title
INTERFEROMETRIC STUDY OF FORCED CONVECTION MASS TRANSFER BOUNDARY LAYERS IN LAMINAR CHANNEL FLOW

Author
Mclarnon, F.R.

Publication Date
1977-08-01

uc-25
uc-4

Submitted to Industrial and
Engineering Chemistry, Fundamentals

LBL-6281 C.1
Preprint

INTERFEROMETRIC STUDY OF FORCED CONVECTION MASS TRANSFER BOUNDARY LAYERS IN LAMINAR CHANNEL FLOW

F. R. McLarnon, R. H. Muller, and C. W. Tobias

August 11, 1977

Prepared for the U. S. Energy Research and
Development Administration under Contract W-7405-ENG-48

INTERFEROMETRIC STUDY OF FORCED CONVECTION MASS TRANSFER BOUNDARY LAYERS IN LAMINAR CHANNEL FLOW

by

F. R. McLarnon*, R. H. Muller and C. W. Tobias

Materials and Molecular Research Division
Lawrence Berkeley Laboratory
and Department of Chemical Engineering
University of California
Berkeley, California 94720

ABSTRACT

Double beam interferometry has been used to determine the development of local mass-transfer boundary layers under laminar flow conditions. A traveling, dual-emission laser interferometer has been employed in the study of a model transfer process, the electrodeposition of copper from copper sulfate solution in a flow channel of rectangular cross section. Concentration profiles in the boundary layer have been derived from experimental interferograms which were corrected for optical aberrations. Mass balance considerations were used to select the correct concentration contour from those associated with practically indistinguishable interference fringes. Asymptotic solutions to the convective diffusion equation have been found to closely describe the transient growth and steady state behavior of laminar, forced convection boundary layers.

---

*Present Address: Department of Chemical Engineering, University of California, Davis, CA 95616.

INTRODUCTION

Mass transport often limits the rate of chemical processes. Many industrially important electrochemical reactions fall in this category; some are also used to model transfer processes. The limiting current technique (Selman, 1971) is an established method for the experimental analysis of problems involving ionic transport to and from electrodes. However, this method gives no direct information about the nature of mass-transfer processes at current densities of practical significance, i.e., below the limiting current, and, even with sectioned electrodes, provides only average steady-state mass transfer rates.

Interferometry (Muller, 1973, Hauf et al., 1970) provides direct continuous visualization of the local concentration boundary layer at any current level. In this technique, point-to-point variations in the phase of transmitted light are measured and the corresponding variations in refractive index (or concentration) are derived from the observation. The interferometric technique offers a unique opportunity to examine the transient and steady-state concentration profile in mass-transfer boundary layers. Of particular interest are the local mass-transfer rate (current density), interfacial concentration and boundary layer thickness. Quantitative information on one-dimensional local concentration fields and qualitative information on two-dimensional local concentration fields (such as those occurring in combined forced and free convection) can be obtained.

Note that our interferometric system (Beach et al., 1969) can also resolve concentration variations along the electrode surface, either in a single interferogram or by moving the interferometer along the length of the flow channel, which results in the determination of three-dimensional concentration fields. Table I compares some characteristics of the interferometric and limiting current methods. The interferometric technique cannot be employed, at present, to resolve the separate concentration gradients when supporting (excess non-reacting) electrolyte is used.

Interferograms shown in Figure 1 illustrate the growth of the steady-state mass-transfer boundary layer with increasing distance downstream from the leading edge. Although these interferograms are distorted due to light-deflection effects (see Appendix I), pertinent qualitative information can be gleaned from the interferograms: (a) the fact that the slope of the fringe contours at the apparent interface is quite similar at the three positions suggests that the current density is uniform along the cathode surface; (b) the boundary layer grows thicker with increasing distance from the cathode leading edge; (c) the concentration difference between bulk solution and interface increases in the downstream direction. (There are 18 fringe shifts at z = 5 cm and 46 at z = 80 cm.) Quantitative interpretation of interferograms requires extensive computations, as outlined in Appendix I.

The present investigation is concerned with the study of mass-transfer boundary layers formed by the electrodeposition of Cu from 0.1 M $CuSO_4$

electrolyte at a downward-facing cathode, embedded in the walls of a rectangular duct flow channel, in laminar flow. Double-beam interferometry is employed to measure the electrolyte concentration changes induced by a controlled change in current density. We also seek to define the practical limits of resolution of interferometry as applied to large-scale systems. The ultimate goal in this research program is to examine mass transfer limitations in electrochemical reactors and investigate practical means to increase reactor space-time yield.

This study complements the work of Tobias and Hickman (1965), that employed the limiting current technique to study ionic mass transport by combined free and forced convection, and the classical heat transfer study of Norris and Streid (1940). Compared to the previous interferometric study by Lin, Moulton and Putnam (1953) on turbulent flow, this investigation accounts for optical aberrations (Muller, 1973; Hauf et al, 1970; Howes et al., 1966) associated with interferometry. The most serious optical aberration is caused by light curvature within the refractive index field (boundary layer), which is fully accounted for in the present work. Its importance has also been recognized in interferometric studies of heat transfer by natural convection (Simon et al., 1963).

EXPERIMENTAL PROCEDURES

(1) Flow Channel

Mass-transfer experiments were carried out in a three meter long rectangular duct flow channel, the heart of which is depicted in Figure 2. (Beach, et al., 1969; Beach, 1971; McLarnon, 1975). Gravity feed from a storage tank provides a steady flow of electrolyte. The duct is $w = 1.00$ cm wide and $h = 2.54$ cm high, and the electrodes fully occupy the space between the two parallel optically flat glass sidewalls. One hundred-forty hydraulic diameters ($d_e = 1.44$ cm) of entry length are provided upstream from the $L = 100$ cm long electrodes.

(2) Electrolyte and Electrode Preparation

The 99.999% pure copper electrodes were designed with two goals in mind: (a) the horizontal electrode working surfaces should be flat and smooth, and (b) the test beam should traverse the cell parallel to the working surface. These requirements were met by first polishing a vertical side of each electrode flat and optically smooth. Then, a right angle-polishing jig was used to prepare the electrode working surfaces perpendicular to the reflecting sides. The cell could then be aligned so that the test beam was parallel (to within 0.1°) to the electrode working surface by reflecting the beam from the side under exactly normal incidence (the reflected beam retraced its path back to its source). The working surface profile was flat to within 1μ over 80% of its width. However, the edges were slightly rounded to about 10μ below the level of the center of the surface (McLarnon et al., 1975a; McLarnon, 1975).

The aqueous $CuSO_4$ electrolyte was prepared by mixing reagent grade $CuSO_4 \cdot 5H_2O$ crystals with twice-distilled water in a 25 gallon polyethylene container. The dependence of electrolyte refractive index on $CuSO_4$ concentration was determined with an Abbé critical angle refractometer. Sample concentrations were determined by gravimetric analysis. A least-squares analysis provided the following linear correlation for the refractive index at $\lambda = 632.8$ nm (He - Ne laser), $0 \leq C \leq 0.1$ M $CuSO_4$:

$$n = 1.33110 + 0.0290 \cdot C \quad . \qquad (1)$$

All electrolysis experiments employed 0.1 M $CuSO_4$ electrolyte.

(3) Interferometer

A cross-section of the duct and dual-emission laser interferometer is shown in Figure 3. A He-Ne laser was modified to emit light from each end, and the interferometer was mounted on a lathe bed to permit travel of the instrument along the length of the electrodes. (Beach et al. (1969); Beach (1971); McLarnon (1975)). The plane of focus (optically conjugate to the film plane of the camera) was located at the inside of the glass sidewall farthest from the camera, x = 0. This is the recommended plane of focus for the observation of cathodic boundary layers in which the refractive index decreases toward the electrode surface (Beach et al., 1973).

The interferometer was first employed to study the pure diffusion, constant-current electrodeposition of Cu from a stagnant layer of 0.1 M $CuSO_4$ onto the downward-facing electrode. For this configuration, the concentration profiles can be accurately predicted by the Sand equation (Sand, 1901; Chapman, et al., 1968) if the diffusivity and transference number of the reacting Cu^{++} ions are known. Effects of optical aberrations and methods developed for their correction can therefore be evaluated (Beach et al., 1973; McLarnon et al., 1976).

The interferometer was subsequently used to investigate the electrodeposition of Cu in forced convection onto the downward-facing electrode. Both the transient growth of the concentration boundary layer and the steady-state concentration distributions were studied under constant applied current (galvanostatic) conditions.

TRANSPORT THEORY

(1) Current Distributions

An exact prediction of current distribution on an electrode requires the knowledge of the local electric field, concentration profile and kinetic behavior of the surface reaction.

The primary current distribution is derived by considering only the electric field between anode and cathode, i.e. uniform electrode potentials are assumed. For the flow channel used here, the primary current density, computed according to Newman (1973; see also Wagner, 1951) is uniformly distributed to within 1% over 98% of the electrode surface (Figure 4,"limited by ohmic drop"). If surface kinetics of the electrode reactions are also taken into account, the secondary current distribution is obtained, which does not display the infinite current density indicated at $z = 0$ and $z = L$ for the primary distribution. Taking the effect of transport processes also into consideration, one obtains the tertiary current distribution. As long as the interfacial electrolyte concentration does not approach zero, the effects of concentration changes at the surface are negligible compared to the ohmic and kinetic effects; for a long flow channel with closely-spaced electrodes, practically uniform current distribution will previal. On the other hand, if the interfacial cupric ion concentration approaches zero everywhere along the length of the electrode (limiting current distribution), concentration polarization effects dominate over ohmic and kinetic effects; the current distribution then decreases in the downstream direction (Figure 4, "limited by convection and diffusion").

The current density in electrochemical systems is directly related to the concentration gradient of the reacting ion at the interface

$$i = \frac{mFD}{1-t_+} \circ \left. \frac{\partial C}{\partial y} \right|_{y=0} = \frac{mFD}{1-t_+} \circ \frac{\Delta C}{\delta_N} , \qquad (2)$$

where δ_N is the equivalent (Nernst) boundary layer thickness over which the concentration change $\Delta C = C_b - C_s$ is manifest. [See the Nomenclature section for the definition of the remaining terms in eq. 2.] Measurement of the total current in an electrochemical cell allows the establishment of a mass balance and thus may serve as an independent check on the values of ΔC and δ_N derived by interferometry.

(2) Solution of the Convective-Diffusion Equation

The convective-diffusion equation for the coordinate system shown in Figure 2, for constant physical properties D and t_+ can be derived from an expression given by Newman (1973, eq. 17-13)

$$\frac{\partial C}{\partial t} + v\frac{\partial C}{\partial z} = D\left[\frac{\partial^2 C}{\partial x^2} + \frac{\partial^2 C}{\partial y^2} + \frac{\partial^2 C}{\partial z^2}\right] , \qquad (3)$$

where y is the direction normal to the electrode surface, C is the single-salt electrolyte concentration, D is the electrolyte diffusion coefficient and v is the electrolyte velocity (for laminar channel flow, the only non-zero velocity component is along the z-direction). For aqueous electrolytes at room temperature, the Schmidt Number is large (approx. 2000) and therefore the mass-transfer boundary layer is much smaller than the hydrodynamic boundary layer. Consequently the derivative $\partial^2C/\partial y^2$ will be the dominant term on the right-hand side of eq. 3, and the electrolyte velocity within the concentration boundary layer can be assumed a linear function of y, $v = \beta y$.

For steady-state laminar flow between two parallel plates, the convective-diffusion equation then becomes

$$\beta y \frac{\partial C}{\partial z} = D \frac{\partial^2 C}{\partial y^2} \qquad (4)$$

with boundary conditions

$$C = C_b \text{ at } z = 0 \tag{4a}$$

$$C = C_b \text{ as } y \to \infty \tag{4b}$$

$$\frac{\partial C}{\partial y} = \gamma \text{ at } y = 0 \tag{4c}$$

With eq. 2, the concentration gradient γ at the interface can be written as:

$$\gamma = \frac{i(1-t_+)}{mFD} \tag{4d}$$

Neither the simplified form of the convective diffusion equation (eq. 4) nor any of the boundary conditions accounts for variations of physical properties D and t_+ with electrolyte concentration. γ will be assumed to be independent of z (uniform current density).

As suggested by Newman (1974), eq. 4 can be solved in terms of a similarity variable η

$$\eta = y \left(\frac{\beta}{9Dz}\right)^{1/3} \tag{5}$$

and a concentration defined by

$$C = C_b - \gamma \left(\frac{9Dz}{\beta}\right)^{1/3} \cdot f(\eta) \quad , \tag{6}$$

where f is a function of η only. The solution to eq. 4 can be expressed in terms of a dimensionless concentration

$$\theta = \frac{C - C_s}{C_b - C_s} \tag{7}$$

as

$$\theta = 1 - e^{-\eta^3} + 3\eta \int_{\eta}^{\infty} x e^{-x^3}\, dx \quad , \tag{8}$$

where

$$C_b - C_s = \Delta C\ (z) = \frac{1}{\Gamma\left(\frac{2}{3}\right)} \left(\frac{9Dz}{\beta}\right)^{1/3} \quad . \tag{9}$$

Equation 9 can be derived directly from Equation (113-2) given by Newman (1973).

For laminar flow between infinitely wide parallel plates, the interfacial velocity gradient takes on a simple form:

$$\beta_\infty = \frac{6\ \overline{v}}{h} \quad , \tag{10}$$

and the equivalent duct diameter d_e is twice the electrode spacing $d_e = 2h$. By use of the following dimensionless groups

$$\mathrm{Nu}\ (z) = \frac{i d_e (1-t_+)}{mFD \cdot \Delta C(z)} = \frac{d_e}{\delta_N(z)} \quad , \tag{11}$$

$$\mathrm{Re} = \frac{\overline{v} \cdot d_e}{\nu} \quad , \tag{12}$$

and

$$\mathrm{Sc} = \frac{\nu}{D} \quad , \tag{13}$$

the concentration distribution eq. 9 can be expressed as

$$\mathrm{Nu}\ (z) = 1.4904 \left(\mathrm{Re} \cdot \mathrm{Sc} \cdot \frac{d_e}{z}\right)^{1/3} \quad . \tag{14}$$

If the more commonly-used boundary condition of constant concentration at the interface ($C = C_s$ at $y = 0$, potentistatic operation) is used in place of the constant concentration gradient boundary condition (eq. 4c, galvanostatic operation), then eq. 15 is obtained (Newman, 1973; Rousar et al. 1971). Note that the transport rate distributions have the same form but differ only in the value of the numerical constant.

$$\mathrm{Nu}\,(\dot{z}) = 1.2325 \left(\mathrm{Re} \cdot \mathrm{Sc} \cdot \frac{d_e}{z}\right)^{1/3} . \tag{15}$$

The dimensionless concentration profiles for constant interfacial concentration then have the form

$$\theta = \frac{1}{\Gamma\left(\frac{4}{3}\right)} \int_{\delta}^{\eta} e^{-x^3}\, dx, \tag{16}$$

which is somewhat different from the constant current profile, eq. 8.

Figure 5 presents a comparison of the two theoretical concentration profiles eqs. 8 and 16. The theoretical profiles were computed with the use of integral tables (Abramowitz, 1964) and both were normalized to give the same slope $d\theta/dY = 2$ at $Y = 0$, where $Y = y/\delta$ is a normalized distance from the electrode surface. This normalization also allows comparison of the two theoretical profiles with two polynomial profiles; a parabolic profile

$$\theta = 2Y - Y^2 \quad , \tag{17}$$

and a Pohlhausen-type profile (Schlichting, 1968)

$$\theta = 2Y - 2Y^3 + Y^4 \quad . \tag{18}$$

Equations 17 and 18 are also plotted in Figure 5. All four curves have been normalized to show the same interfacial slope. The Pohlhausen-type profile eq. 18 is practically indistinguishable from the constant-current theoretical profile eq. 8.

(3) Average Velocity Gradient

The above solution of the convective diffusion equation was based on a constant value for the interfacial velocity gradient β, corresponding to infinitely wide parallel plates (eq. 10). In a flow channel of finite width β will, however, vary in the x-direction due to the effects of the glass sidewalls on the electrolyte flow profile. An average value of β is required to compute the appropriate theoretical concentration variation from eq. 9. The form of eq. 9 suggests the following average:

$$\langle \beta^{-1/3} \rangle = \frac{1}{W} \int_0^W \beta^{-1/3}\, dx. \tag{19}$$

Rousar et al. (1971) have used

$$\langle \beta^{1/3} \rangle = \frac{1}{W} \int_0^W \beta^{1/3}\, dx \tag{20}$$

for a similar computation. The velocity gradients were calculated by the method of Love, (1927) as illustrated by Rousar et al. (1971). Figure 6 depicts the computed ratio $\beta(x)/\beta_\infty$ as a function of reduced horizontal distance in the duct.

Standard formulae e.g., Newton-Cotes closed-end quadrature (listed by Lapidus, 1962) were used to evaluate eqs. 19 and 20, and the corresponding dimensionless Nusselt Number distribution was calculated using the equivalent duct diameter d_e:

$$d_e = \frac{2\ hw}{h + w} \quad . \tag{21}$$

The resulting Nusselt Number distributions are identical to eq. 14 save for the numerical constant, as summarized in Table II.

The effects of the velocity gradient variation (shown in Figure 6) are illustrated schematically in Figure 7. The concentration boundary layer is expected to be thicker near the edge of the electrode (x = 0 or x = W) where the velocity approaches zero, and there would be a thinner boundary layer near the center of the electrode where the velocity gradient is at a maximum. Because the electrodes occupy the entire space between the glass walls, the primary current distribution in the x-direction is uniform. Inspection of eq. 2 shows that the concentration change $\Delta C\ (x)$ and Nernst boundary layer thickness $\delta_N\ (x)$ should vary in exact proportion (neglecting physical property variation). Eqs. 9 and 19 relate the concentration change and boundary layer thickness to the local velocity gradient. This relationship can be expressed as a dimensionless function $Q\ (x)$:

$$Q\ (x) = \frac{\beta^{-1/3}\ (x)}{\langle \beta^{-1/3} \rangle} = \frac{\Delta C(x)}{\langle \Delta C \rangle} = \frac{\delta_N\ (x)}{\langle \delta_N \rangle} \quad . \qquad (22)$$

Equation 22 is plotted as the solid curve in Figure 8, which demonstrates that the concentration boundary layer might be expected to grow without limit at $x = 0$ and $x = W$. This anomaly arises because diffusion in the x-direction is not accounted for in eq. 4.

Of course, the boundary layer thickness is not infinite at the glass wall and the profile must be bounded by the two extreme cases: that depicted by the solid curve in Figure 8 and that for a uniform layer thickness ($Q = 1$) associated with laminar flow between infinitely wide parallel plates. The appropriate numerical factor in the Nusselt Number distribution for steady-state, constant-current electrodeposition must then lie between the two extreme numbers tabulated in Table II: $\phi = 1.4904$, which corresponds to infinitely wide parallel plates, and $\phi = 1.112$, which corresponds to the duct dimensions shown in Figures 2 and 3. Note that different means to average the velocity gradient β, resulting in eqs. 19 and 20, have little effect on ϕ. The value of ϕ actually used to evaluate the Nusselt Number distribution was $\phi = 1.2325$, which lies between the two extreme values (1.112, 1.4904), corresponding to constant current conditions. The chosen value of ϕ has been derived for constant interfacial concentration by Newman (1973) and is shown as the last entry in Table II.

(4) Computation of Steady-State Boundary Layer

In order to compare experimentally-determined interfacial concentration (e.i., $\Delta C(z)$) and boundary layer thickness ($\delta_N(z)$) with theoretical expectation, eqs. 11 and 15 must be used. Over the range of concentrations of interest, the variation in physical properties should be accounted for. Between 0 and 0.1 M $CuSO_4$ the electrolyte diffusion coefficient D shows a 40% variation (Eversole et al., 1942), and the cation transference number t_+ exhibits a 10% variation (Fritz et al., 1958). There is also a possible ± 10% uncertainty in the value of the electrolyte diffusion coefficient at a given concentration. The values of diffusion coefficients were corrected from 25°C to 20°C (ambient) and corresponded to the local interfacial concentration $C_s(z)$. The value of electrolyte kinematic viscosity ν used in the computation of Reynolds Number $Re = \bar{v}d_e/\nu$ and Schmidt Number $Sc = \nu/D$ was taken from the compilation of Chapman and Newman (1968) and assumed invariant with electrolyte concentration (valid to within 5.6% for $0 \leqslant C \leqslant 0.1$ M $CuSO_4$).

Please note that we account for physical property variations by choosing values for D and t_+ which correspond to the local interfacial concentration, although a closed-form solution to the convective-diffusion equation, valid for constant physical properties, is used. The error incurred by this simplified procedure is likely to be less than that caused by the possible 10% error in diffusion coefficient (Selman, 1971).

(5) Computation of Transient Boundary Layer

The entire equation of convective diffusion (eq. 3) must be solved in order to find the exact transient concentration profiles. Rather than to deal with the mathematical difficulties involved in such a solution, it might be preferable to find asymptotic solutions. For sufficiently short times after current switch-on, the concentration variations will be confined to a relatively thin (e.g., one-tenth of the steady-state boundary layer thickness) layer right at the electrode surface. The local concentration gradient ($\partial C/\partial y$) will depend only upon the local current density because there will have been insufficient time for upstream regions of depleted electrolyte to flow downstream and affect the concentration variations there. Since the current is expected to be distributed quite uniformly along the length of the electrode, the concentration variations should be independent of the location z along the electrode. The term ($\partial C/\partial z$) in eq. 3 can then be neglected, and the convective-diffusion equation reduces to

$$\frac{\partial C}{\partial t} = D\frac{\partial^2 C}{\partial y^2} , \tag{23}$$

with the boundary conditions

$$C = C_b \text{ at } t = 0 \tag{24a}$$

$$C = C_b \text{ as } y \to \infty \tag{24b}$$

$$\frac{\partial C}{\partial y} = \frac{i\ (1-t_+)}{mFD} \text{ at } y = 0 \tag{24c}$$

for which the solution is well known (Sand, 1901).

$$\theta = 1 + y \cdot \sqrt{\frac{\pi}{4Dt}} \cdot \operatorname{erfc}\left(\frac{y}{\sqrt{4Dt}}\right) - \exp\left(\frac{-y^2}{4Dt}\right) \qquad (25)$$

$$\Delta C = \frac{2i\ (1-t_+)}{mF} \cdot \sqrt{\frac{t}{\pi\ D}} \qquad (26)$$

We have previously reported good agreement between the interferometrically determined transient concentration changes in the absence of convection and those predicted by Eq. 26 (McLarnon et al., 1976).

RESULTS AND DISCUSSION

The iterative technique used to derive concentration profiles from experimental interferograms employed two model concentration functions, a polynominal profile

$$\theta = 1 - (1 - kY)^2(1 - Y^2) \quad \text{with } -0.268 \leqslant k \leqslant 1.0\,, \qquad (27)$$

and a generalized Pohlhausen-type profile

$$\theta = KY + (4 - 3K)Y^3 + (2K - 3)Y^4 \quad \text{with } \frac{4}{3} \leqslant K \leqslant 2. \qquad (28)$$

These functions are further discussed in Appendix I.

(1) Transient Behavior

The transient growth of laminar forced-convection mass transfer boundary layers was investigated to determine the effects of electrolyte flow rate, level of applied current density and position downstream from the cathode leading edge. The experimental interferograms were analyzed as outlined in Appendix I. The local one-dimensional concentration fields were approximated by eq. 27 which had been used successfully in the absence of convection. The transient concentration differences ΔC between bulk solution and interface, derived from the observations, are plotted in Figures 9 and 10. The sloped lines represent the behavior in the absence on convection (eqs. 25, 26 which is also the short-term asymptotic solution of the convective diffusion equation - eq. 3). Constant physical properties D and t_+ (Eversole et al, 1942, Fritz et al., 1958), corresponding to the bulk electrolyte concentration $C_b = 0.1$ M $CuSO_4$ were employed in the evaluation of eq. 26, which should be a good approximation because concentration changes for short times are small.

The horizontal lines represent the long-term asymptotic (steady-state) solution (eq. 15) to the convective diffusion equation. The measured points follow the two asymptotic solutions closely. Note that the transition from short-term to long-term behavior is surprisingly sharp. The minimum transition time t to steady-state corresponds to the intersection between the two asymptotic solutions (solid lines) on Figures 9 and 10. Using the value of t and the steady-state Nernst boundary layer thickness computed from eqs. 9 and 11, we can calculate the dimensionless transition times τ (Bird et al., 1959) shown in Table III.

$$\tau = \frac{Dt}{\delta_N^2} \tag{29}$$

The characteristic diffusion time τ can also be computed by eliminating δ_N, i and ΔC between eqs. 2, 26 and 29. For a constant diffusion coefficient, one obtains $\tau = \pi/4 = 0.785$. The deviations (below $\tau = \pi/4$) seen in Table III are due to the variations in physical properties that have been incorporated in the computations for the steady-state concentration differences, but are not considered in the short-term asymptotic solution.

Table IV lists the interferometrically derived transient current densities and curve shape parameters for the experiments shown in Table III. The derived currents show general agreement with the applied currents for short times. (The first entry is likely to be in error because of the very thin boundary layer.) For long times, the derived currents are consistently high. This is an indication that the polynominal function eq. 27 is successfully fitting the actual concentration profiles at shorter times but not at longer times. The derived curve shape parameter k is also listed in Table IV. For short times, k is closer to unity, while for long times, k is closer to zero. This corresponds to a change in the functional form of the concentration field from approximately a fourth order polynomial profile (k = 1, eq. 27) to approximately a second order profile (k = 0), as steady-state conditions are approached. The success of the polynominal function eq. 27 in describing the short time concentration profiles should be expected: The mass transfer process is diffusion controlled, and the polynominal function proves quite adequate in the analysis of transient diffusion layers. However, eq. 27 apparently does not describe well the steady-state concentration profiles. This will be discussed more fully later.

(2) Steady-State Behavior

Preliminary attempts at a quantitative interpretation of experimental interferograms of steady-state boundary layers, such as those shown in Figure 1, employed the polynominal function (eq. 27) to describe the concentration field. Although it was possible to find computed interferograms showing excellent agreement with all experimental interferograms, the derived current densities were consistently 20-30% higher than the level of applied current. This is in marked contrast to the analysis of transient diffusion layers, where the derived currents showed good agreement with applied currents.

Several factors have been investigated as a possible cause of the discrepancy between the applied current density and that derived from the optical analysis: (a) The fitting function could not adequately describe the real concentration profile; (b) variation of boundary layers across the flow channel (i.e. in the x-direction, Figure 2); (c) uncertainty in the location of the electrode surface on the interferogram. The last source of error was judged to be small because of the previous success in interpreting concentration profiles in the absence of convection. The first two sources will be discussed below.

In order to investigate the effect of a different fitting function for the concentration profile, a Pohlhausen-type profile (eq. 28) was used. At the same time, the effect of boundary layer variations across the channel were accounted for. As can be seen in Table V, the current density derived from the use of a Pohlhausen profile agrees closely with the applied current density, in contrast to the use of a polynomial function, which resulted in consistently too high current densities (steady state results in Table IV). The derived current densities, interfacial concentrations and boundary layer thicknesses are very weakly dependent on possible variations in the boundary layer across the channel. Note that in all cases, good agreement is obtained between computed and observed interference fringes. A slight disagreement between the fit resulting from the use of one or two-dimensional concentration profiles is discussed in Appendix II.

A conclusion of this analysis is that the match between computed and experimental interferogram is not sufficiently sensitive to guarantee that a unique concentration field has been determined. In the present study, a choice between possible fitting functions has been made by considering an additional constraint. An overall cupric ion mass balance has been satisfied by requiring that the optically derived current density agree with the applied current density. A complete analysis of this problem and recommendations for surmounting it have been presented by McLarnon et al., 1975, c.

Figures 11 and 12 compare interferometrically derived current densities with applied currents. The filled symbols represent conventional interpretation of the experimental interferograms (eq. 31,

Appendix I). The open symbols correspond to interferogram analysis using the two-dimensional Pohlhausen-type boundary layer profile, eq. 28. At lower current densities (i.e. less than 2 mA/cm^2) conventional analysis of the experimental interferograms gives results not unlike those from the detailed analysis. At higher current densities, however, conventional analysis would lead to erroneous conclusions. For example, the closed triangles in Figure 12 would indicate (a) local currents 20-60% lower than the applied current $i = 5\text{mA/cm}^2$ and (b) local current densities increasing in the direction of flow. The low current densities would violate mass balance considerations, and the apparent current distribution is contrary to both the primary and tertiary current distributions shown in Figure 4.

The anomalous current distribution derived by simple analysis of the experimental interferograms could have been predicted by the light-deflection error correlation shown previously (Figure 10, McLarnon, et al., 1975, b). That correlation shows that the interfacial refractive-index gradient (current density) derived from an interferogram in the conventional way is likely to be lower than the true gradient. Moreover, the derived current densities will be lower (i.e. the light-deflection error is more severe) for smaller concentration differences ΔC, and vice-versa. This latter effect is the cause of the false current distribution; the apparent current density is lower near the cathode leading edge where ΔC is smaller and higher near the cathode trailing edge where ΔC is larger.

Figures 13-15 show that the average boundary layer thicknesses and concentration changes derived, using the two-dimensional Pohlhausen-type boundary layer profile eq. 28, agree with theoretical predictions. The discrepancy between derived and predicted ΔC at $z = 0.5$ cm seen in Figures 14 and 15 is caused by the higher than average current density near the cathode leading edge $z = 0$ (primary current distribution, Figure 4). Table VI catalogues derived values of the curve shape parameter K (eq. 28) associated with the interferometric results presented in Figs. 11-15. The derived values cluster about $K = 2.0$, which corresponds to the Pohlhausen profile eq. 28. Figure 5 illustrates the close agreement between the Pohlhausen profile and the theoretical profile eq. 8 for constant-current electrodeposition. The unsuccessfuly polynomial profile eq. 27 would correspond to the parabolic profile eq. 17 shown in Figure 5.

The preceding paragraph points out an important concept in the design of interferometric experiments. To avoid distortions due to light-deflection effects, one must consider refractive-index gradients, specimen size and refractive-index differences. For instance, a small interfacial refractive-index gradient ($i \approx 1$ mA/cm^2) does not guarantee negligible light-deflection errors. The interferometric study of forced convection boundary layers by Lin et al. (1953) is a case in point. This work employed a Mach-Zehnder interferometer (Hg arc light source, $\lambda = 546$ nm) to observe the mass-transfer boundary layer formed by the electrodeposition of Cd from 0.01 M $CdSO_4$ electrolyte in a 3.17 cm wide flow channel. Table VII lists the results of a conventional analysis of three different interferograms presented in the Ph.D. dissertation of C. S. Lin (1952). This computation of current densities from the experimental interferograms required knowledge of the relation between changes in electrolyte concentration and changes in refractive-index; the value dn/dC = 0.29 M^{-1} (see eq. 1) for $CuSO_4$ was used for this purpose. Durou et al. (1973) measured the refractive-indices of aqueous solutions of $CuSO_4$, $ZnSO_4$ and other electrolytes, and their results indicate that dn/dC = 0.029 ± 0.001 for either $CuSO_4$ or $ZnSO_4$, $0 \leqslant C \leqslant 0.1$ M. Therefore, it is not unreasonable to use this same value for dilute $CdSO_4$ electrolyte. Current densities were computed from the interferometrically derived concentration gradients, using eq. 2 and the values $D = 7.9 \times 10^{-6}$ cm^2/s and $t_+ = 0.40$ for 10^{-2} M $CdSO_4$ given in the compilation of Chapman and Newman (1968). These values correspond to an effective diffusion coefficient

$$D_{eff} = D/(1 - t_+) = 1.3 \times 10^{-5} \text{ cm}^2/\text{s} \qquad (30)$$

which is 30% higher than that used by Lin et al. (1953): $D_{eff} = 10^{-5}$ cm^2/s.

Table VII shows that the apparent current density is smaller than the applied current for experiments 69 and 71, and the current densities show good agreement for experiment 79. These observations are consistent with the light-deflection errors predicted by McLarnon et al. (1975, b): the error is more severe for higher current densities and smaller concentration differences. Even though small current densities were used, the wide (3.17 cm) cell and small concentration differences (<0.01M) resulted in significant light-deflection errors.

CONCLUSION

The derivation of concentration profiles in boundary layers from interferograms has been shown to require the consideration of the deflection (bending) of light in the boundary layer and the possible reflection from the electrode. Completely erroneous conclusions may otherwide be obtained. In addition, it has been demonstrated that interferometric measurements may not be amenable to a unique interpretation. Application of an overall mass balance (agreement between measured and optically derived current density) permitted a rational choice between different concentration contours associated with optically indistinguisable interference fringes. On this basis a Pohlhausen-type function was found to best describe the concentration profile in boundary layers under steady state laminar forced convection. The derived local concentrations, gradients and boundary layer thicknesses agree with theoretical predictions to within ± 10%.

The transient growth of convective boundary layers can be well described by asymptotic solutions to the convective diffusion equation. The short-term behavior is identical to that in the absence of convection; the transition to steady-state behavior has been found to be surprisingly abrupt.

APPENDIX I

OPTICAL ANALYSIS

The conventional interpretation of interferograms is based upon the assumption that light rays propagate along straight lines as they traverse the specimen. Phase (N = number of fringe shifts) on the interferogram is then directly related to a local refractive-index difference $\Delta n = n_b - n_s$ within the specimen

$$\Delta n = \frac{N\,\lambda}{W}\,, \tag{31}$$

which can be related to local concentration using eq. 1. However, the light rays will be deflected (refracted) as they traverse the refractive-index field. Figure 16 illustrates the trajectory ABC of a deflected ray as it traverses a cathodic concentration boundary layer of thickness δ. The deflected ray appears to emanate from its virtual origin D in the virtual plane of focus DE. This effect causes the receding of the electrode shadow from its true location ($y = 0$), shown in Figure 1.

Previous studies (Beach et al., 1973; McLarnon et al., 1975, b) have demonstrated that large errors can result if interferograms are interpreted in the conventional way, i.e., ignoring the refraction effect. Correlations of light-deflection errors for various values of specimen width w, refractive-index differences Δn, and interfacial refractive-index gradients (current densities) have been presented elsewhere (McLarnon et al., 1975, b).

Another optical aberration in interferometry is caused by reflection from the edge of the solid surface (McLarnon et al., 1975, a). Light rays reflected from the even slightly rounded edge of the electrode surface can produce significant distortions in the experimental interferogram. Figure 17 presents four separate experimental fringe patterns of the interface between homogeneous 0.1 M $CuSO_4$ electrolyte and a carefully polished copper electrode. Interferometric distortions caused by edge-reflection share characteristics with those caused by refraction: (a) the magnitude of the distortion depends upon the location of the plane of focus, and (b) the apparent interface (electrode shadow) can be different from the true location $y = 0$. Note that there are no refractive-index gradients in the electrolyte, but reflection causes an anomalous fringe bending which is more pronounced for focus at $x \leqslant 0$.

An iterative technique is required to derive quantitative-concentration profiles (refractive-index fields) from experimental interferograms. (McLarnon et al., 1975, c; McLarnon, 1975). A summary of the steps involved is given here:

1. Guess a concentration profile. Two different functions were used, a polynomial profile, eq. 27, and a generalized Pohlhausen-type profile, eq. 28. The limits on the parameters k and k insure that the dimensionless functions eqs. 27 and 28 demonstrate no inflection or extremum

in the range $0 < Y < 1$, where $Y = y/\delta$ is a reduced distance. Note that the parabolic profile eq. 17 is a special case of eq. 27 for $k = 0$ and the Pohlhausen profile eq. 18 is a special case of eq. 28 for $K = 2$. Both eqs. 27 and 28 have three variable parameters, δ, C_s (or n_s) and k (or K).

2. Compute the interferogram associated with the guessed concentration profile. Part of the calculation requires the trajectories $y(X)$ and optical path lengths $p(w)$ of many (10-40) deflected rays AB (Figure 16) as they traverse the boundary layer. The trajectory $y(x)$ is found by solving the equation of light-deflection

$$\frac{d^2y}{dx^2} = \frac{1}{n(x,y)} \left[1 + \frac{dy}{dx}^2\right] \left[\frac{\partial n}{\partial y} - \frac{dy}{dx} \frac{\partial n}{\partial x}\right] \tag{32}$$

with

$y = y_e$ at $x = 0$,

$\frac{dy}{dx} = 0$ at $x = 0$,

and the optical path length of ray AB if found by performing the quadrature

$$p(w) = \int_0^w n\,(x,y)\ \sqrt{1 + \frac{dy}{dx}^{2}} \qquad (33)$$

concurrently with the solution of eq. 32.

For a one-dimensional refractive-index field, n = n (y) only, a closed-form solution to eq. 32 is possible for the refractive-index function eq. 27. Complete details of this solution are given by McLarnon et al. (1975, c). For a two-dimensional refractive-index function n = n(x,y), a tedious numerical solution (Beach et al is required. The variations $\Delta C(x)$ and $\delta_N(x)$ are taken into account as indicated by eq. 22, where an approximate form for Q(x) is employed, illustrated by the dashed curve in Figure 8. This approximation avoids the infinite layer thickness at x = 0 and x = w (zero velocity gradient β) by arbitrarily assigning the value Q(w) = Q(0) = 2.5.

3. Compare the computed interferogram with the experimental one by calculating the standard and average deviations between the two contours. It was found that an efficient iteration routine resulted from adjusting the interfacial concentration until zero average deviation was obtained and by adjusting the curve shape parameters to minimize the standard deviation.

If the fit is not satisfactory, repeat step (2), using different parameters, until a fit is found. Up to 80 iterations may be required.

4. Repeat steps (1) - (3) for several slightly different interfacial positions (e.g., change the measured location $y = 0$ by ± 0.01 mm). As indicated by Figure 17, there may be difficulty in locating the precise interfacial location, and this step permits determination of likely errors incurred.

APPENDIX II

ONE AND TWO-DIMENSIONAL BOUNDARY LAYERS

The Pohlhausen-type boundary layer profile, eq. 28, was employed to analyze the interferograms of steady-state boundary layers for one-dimensional, $C = C\ (y)$, and two-dimensional, $C = C\ (x,y)$, concentration fields. We have previously pointed out that the results in Table IV indicate little difference between values of i, K, ΔC and δ_N derived from the experimental interferograms by the two different methods. There is, however, a slight difference between the interferograms computed by using one- or two-dimensional concentration fields as illustrated in Figure 18. Figure 18a shows a one-dimensional analysis of the experimental interferogram of the steady-state concentration boundary layer at $z = 79.5$ cm for $Re = 590$ and $i = 1.5\ mA/cm^2$. The computed interferogram, identified by the solid curve, passes below the three uppermost data points (fringe shifts on the experimental interferogram, the uppermost point is at $y = 0.85$ mm). Figure 18b depicts the two-dimensional analysis of the same interferogram; the computed fringe passes above only the uppermost point. These small deviations are also characteristic of the other experiments listed in Table V and can be explained in terms of the thicker than average mass transfer boundary layer right at the glass sidewall. The one-dimensional analysis Figure 18a cannot account for this effect, so the edge of the boundary layer (three uppermost data points) appears to extend somewhat higher than the computed (average) boundary layer edge. The two-dimensional analysis can account for this effect, but the observed boundary layer edge (uppermost data point in Figure 18b) appears somewhat lower than the computed edge. This is an indication that the approximate boundary layer cross-channel variation (indicated by the dashed curve in Figure 8) might be too strong; a more perfect agreement between computed and experimental interferograms would be possible by use of a more moderate boundary layer variation.

NOMENCLATURE

C	electrolyte concentration (mole/liter)
C_b	bulk concentration (mole/liter)
C_s	interfacial concentration (mole/liter)
d_e	equivalent duct diameter (cm)
D	diffusion coefficient (cm^2/s)
f	similarity function, see eq. 6
F	Faraday constant (coul/eq)
h	anode-cathode spacing (cm)
i	current density (A/cm^2)
k	fitting parameter, see eq. 27
K	fitting parameter, see eq. 28
L	electrode length (cm)
m	cation valence, see eq. 2
n	electrolyte refractive-index
n_b	bulk refractive-index
n_s	interfacial refractive-index
N	phase (fringe shifts)
Nu	Nusselt number
p	optical path length (cm)
Q	see Figure 8, eq. 22
Re	Reynolds number
Sc	Schmidt number
t	time(s)
t_+	cation transference number

v	electrolyte velocity (cm/s)
$\bar{v}$	volume average electrolyte velocity (cm/s)
w	electrode width (cm)
x	horizontal (cross-channel) direction (cm)
y	vertical direction (cm)
y_e	position where a light ray enters the electrolyte (cm)
Y	dimensionless vertical distance y/δ
z	distance from electrode leading edge in the flow direction (cm)
β	interfacial velocity gradients(s^{-1})
β_∞	interfacial velocity gradient, $h/w \to 0$ (s^{-1})
γ	interfacial concentration gradient (M/cm)
δ	boundary layer thickness (cm)
δ_N	Nernst boundary layer thickness (cm)
ΔC	concentration difference $C_b - C_s$ (mole/liter)
Δn	refractive-index difference $n_b - n_s$
η	similarity variable, see eq. 5
θ	dimensionless concentration, $(C - C_s)/(C_b - C_s)$
λ	light wavelength (nm)
ν	electrolyte kinematic viscosity (cm^2/s)
τ	dimensionless time, see eq. 29
ϕ	constant, see Table II.

REFERENCES

Abramowitz, M. and Stegun, I., eds., Handbook of Mathematical Functions, National Bureau of Standards, Washington, 1964, pp. 255-262, 320.

Beach, K. W., Muller, R. N. and Tobias, C. W., Rev. Sci. Instr. 40, 1248 (1969).

Beach, K. W., "Optical Methods for the Study of Convective Mass Transfer Boundary Layers on Extended Electrodes," Ph.D. Thesis, UCRL-20324, Univ. of Calif., Berkeley, 1971.

Beach, K. W., Muller, R. H. and Tobias, C. W., J. Opt. Soc. Am. 63, 559 (1973).

Bird, R. B., Stewart, W. E. and Lightfoot, E., Transport Phenomena, Wiley, New York, 1960, p. 354.

Chapman, T. W. and Newman, J. S., "A Compilation of Selected Thermodynamic and Transport Properties of Binary Electrolytes in Aqueous Solution," UCRL-17767 (1968).

Durou, C. Giraudou, J. C. and Moutou, C., J. Chem. Eng. Data 18, 289 (1973).

Eversole, W. G., Kindsvater, H. M. and Peterson, J. D., J. Phys. Chem. 46, 370 (1942).

Fritz, J. J. and Fuget, C. R., J. Phys. Chem. 62, 303 (1958).

Hauf, W. and Grigull, U. in Advances in Heat Transfer, Hartnett, J. P. and Irvine, T. F., eds., Academic Press, New York, 1970, Vol. 6, pp. 133-366.

Howes, W. L. and Buchele, D. R., J. Opt. Soc. Am. 56, 1517 (1966).

Lapidus, L., Digital Computation of Chemical Engineers, McGraw-Hill, New York, 1962, p. 51.

Lin, C. S., "Mass Transfer Between Solid Wall and Fluid Streams, " Ph.D. Thesis, Department of Chemical Engineering, Univ. of Washington, 1952.

Lin, C. S., Moulton, R. W. and Putnam, G. L., Ind. Eng. Chem. 45, 640 (1953).

Love, A. E. H., Treatise on Mathematical Theory of Elasticity, Cambridge University Press, 1927, p. 129.

McLarnon, F. R., "Interferometry of Electrochemical Mass Transfer Boundary Layers," Ph.D. Thesis, LBL-3500, Univ. of Calif., Berkeley, 1975.

McLarnon, F. R., Muller, R. H. and Tobias, C. W., Appl. Opt. 14, 2468 (1975), a.

McLarnon, F. R., Muller, R. H. and Tobias, C. W., J. Electrochem. Soc., 122, 59 (1975), b.

McLarnon, F. R., Muller, R. H. and Tobias, C. W., J. Opt. Soc. Am. 65, 1011 (1975), c.

McLarnon, F. R., Muller, R. H. and Tobias, C. W., Electrochim. Acta 21, 101 (1976).

Muller, R. H. in Advances in Electrochemistry and Electrochemical Engineering, R. H. Muller, ed., Wiley-Interscience, N. Y., 1973, Vol. 9, pp. 326-353.

Newman, J. S., Electrochemical Systems, Prentice-Hall, Englewood Cliffs, N. J., 1973, pp. 225, 322, 318, 331, 342.

Newman, J. S., private communication (1974).

Norris, R. H. and Streid, D. D., Trans. ASME 62, 525 (1940).

Roušar, I., Hostomsky, J. and Cezner, V., J. Electrochem. Soc. 118, 881 (1971).

Sand, H. J. S., Phil. Mag. 1 (6), 45 (1901).

Schlichting, H., Boundary Layer Theory, McGraw-Hill, N. Y., 1968, p. 291.

Selman, J. R., "Measurement and Interpretation of Limiting Currents," Ph.D. Thesis, UCRL-20557, Univ. of Calif., Berkeley, 1971; also: C. W. Tobias and J. R. Selman, in Advances in Chemical Engineering, Vol. 8, T. B. Drew, J. W. Hoopes, Jr., T. Vermeulen and G. R. Cokelet, eds., Academic Press, New York, in press.

Simon, H. A. and Eckert, E. R. G., Int. J. Heat Mass Transfer 6, 681 (1963).

Tobias, C. W. and Hickman, R. G., Z. Physik. Chemie 229, 145 (1965).

Wagner, C., J. Electrochem. Soc. 98, 116 (1951).

ACKNOWLEDGEMENT

This work was conducted under the auspices of the U. S. Energy Research and Development Administration.

TABLE I

COMPARISON OF THE INTERFEROMETRIC AND LIMITING CURRENT TECHNIQUES

	Interferometry	Limiting Current
Spatial resolution.	high	usually low
Level of current density.	any	limiting current only
Use with supporting electrolyte.	no	yes
Determine boundary layer structure.	yes	no
Analysis of experimental results.	complex	simple
Electrode sectioning required.	no	yes
Observation of transient effects.	yes	no

TABLE II

FACTOR IN NUSSELT NUMBER DISTRIBUTIONS

$$Nu = \phi \left(Re\ Sc\ \frac{d_e}{z} \right)^{1/3}$$

	Computation for β	ϕ
Constant Current	Eq. (10)	1.4904
Constant Current	Eq. (19)	1.112
Constant Current	Eq. (20)	1.166
Constant Potential (Interfacial Concentration)	Eq. (10)	1.2325

TABLE III

DIMENSIONLESS TRANSITION TIMES τ.

Re	i (mA/cm^2)	z (cm)	t (min)	τ
590	1.5	79.5	4.6	0.78
590	3.0	79.5	3.8	0.65
1500	2.5	79.5	2.2	0.68
1500	5.0	5.0	0.36	0.72

TABLE IV

TRANSIENT CURRENT DENSITIES i AND CURVE SHAPE PARAMETERS k DERIVED FROM EXPERIMENTAL INTERFEROGRAMS

Reynolds Number		590		590		1500		1500	
Distance from Leading Edge	(cm)	79.5		79.5		79.5		5.0	
Applied current	(mA/cm^2)	1.5		3.0		2.5		5.0	
	t (min)	i	k	i	k	i	k	i	k
	0.17	1.2	1.00	1.9	0.90	2.5	0.79	4.1	1.00
	0.5	1.4	0.60	2.4	0.82	2.1	0.46	5.6	0.42
	1.0	1.5	0.81	3.0	1.00	2.4	0.84	6.6	0.42
	2.0	1.4	0.43	3.0	1.00	2.6	0.30	---	---
	5.0	1.7	0.18	3.6	0.31	3.1	0.24	---	---
	10.0	1.8	0.19	3.4	0.22	3.3	0.27	---	---
	20.0	1.9	0.28	3.6	0.24	3.1	0.22	6.6	0.48
	30.0	1.9	0.20	3.6	0.25	3.1	0.23	5.9	0.34

TABLE V

INTERFEROGRAM ANALYSIS USING ONE- AND TWO-DIMENSIONAL POHLHAUSEN-TYPE BOUNDARY LAYER PROFILES.

INTERFEROGRAMS OF STEADY-STATE MASS TRANSFER BOUNDARY LAYERS RECORDED AT Z = 79.5 CM.

Applied		Measured				
Re	i	dim.*	i (mA/cm^2)	K	ΔC (M $CuSO_4$)	δ_N (mm)
590	1.5	1	1.51	2.06	0.039	0.415
		2	1.56	2.04	0.040	0.405
590	3.0	1	2.73	2.02	0.067	0.407
		2	2.81	2.00	0.067	0.404
1500	2.5	1	2.41	2.00	0.044	0.296
		2	2.43	1.76	0.044	0.296
1500	5.0	1	4.54	1.98	0.078	0.290
		2	4.73	1.88	0.089	0.289

* Dimension of assumed concentration field.

TABLE VI

DERIVED VALUES OF THE CURVE SHAPE PARAMETER K FOR THE TWO-DIMENSIONAL POHLHAUSEN-TYPE BOUNDARY LAYER PROFILE. EQ. 28

z(cm)	Re = 590 i = 1.5 mA/cm^2	Re = 590 i = 3.0	Re = 1500 i = 2.5	Re = 1500 i = 5.0
0.5	2.46	2.02	2.04	2.07
5.0	1.97	2.04	2.13	2.28
9.5	2.01	2.01	2.05	2.04
19.5	2.01	2.02	1.80	2.08
49.5	2.06	1.90	2.34	1.81
49.5	2.02	2.00	2.06	1.99
79.5	2.04	2.00	1.76	1.88

TABLE VII.

CONVENTIONAL ANALYSIS OF EXPERIMENTAL INTERFEROGRAMS (LIN, 1952).

EXPERIMENT NUMBER	TOTAL NUMBER OF FRINGE SHIFTS (PROPORTIONAL TO ΔC)	APPLIED CURRENT DENSITY	DERIVED CURRENT DENSITY
69	3.24	1.0	0.54
71	3.23	0.44	0.35
79	6.96	0.96	0.97

FIGURE CAPTIONS

Fig. 1 Experimental interferograms showing the growth of the boundary layer in the flow direction.

Ordinate: vertical distance, measured downward from the true electrode/electrolyte interface identified by "0".

The cathode is represented by the black area and is facing down. Actual current density i = 4.5 mA/cm^2.

Fig. 2 Semi-scale drawing of the flow channel. w = 10.0 mm, h = 25.4 mm and L = 100.0 cm.

Fig. 3 Interferometer and electrochemical cell cross section.

——————— Light path

— — — — — Off-axis rays demonstrating point-to-point relationship between plane of focus and film plane

A	Copper anode
C	Copper cathode
E	0.1 M $CuSO_4$ electrolyte
F	Film plane
G	Glass sidewalls
L	Lens. The test lens (focal length 87 mm) is 115 mm from the center of the cell. The focal length of the reference lens is 81 mm.
M	Mirror
S	Light Source (HeNe laser)
U	Beam uniter
d	Thickness of glass wall (12.7 mm)
h	Electrode separation (25.4 mm)
w	Electrode width (10.0 mm)

Fig. 4 Current distributions along the electrode surfaces shown in Fig. 2.

Ordinate: local current density divided by average current density

Abscissa: reduce distance z/L

the primary current distribution is limited by ohmic drop, and the tertiary current distribution eq. 14 is limited by convection and diffusion.

Fig. 5 Dimensionless concentration profiles.

Ordinate: reduced distance

Abscissa: dimensionless concentration

———————— Pohlhausen profile, eq. 18

——— — ——— — Parabolic profile, eq. 17

- - - - - - - Constant interfacial concentration gradient eq. 8

. . . . Constant interfacial concentration eq. 16

Fig. 6 Interfacial velocity gradient

Ordinate: local interfacial velocity gradient $\beta(x)$ divided by that for infinitely wide plates, β_∞ ($h/w \rightarrow 0$, eq. 10).

Abscissa: reduced horizontal distance x/w.

The curve is symmetrical about $x/w = 0.5$.

Fig. 7 Boundary layer variation in the cross-channel direction.

Velocity profiles v: v = 0 at the glass wall and at the electrode surface. Concentration profiles c: The concentration boundary layer is thicker at the glass wall and thinner near the center of the channel.

Fig. 8 Variation of the local boundary layer thickness Q (relative to the average thickness) in the cross-channel direction (x/w = reduced horizontal distance)

——— Computed by the method of Love(1927).

— — — — Approximation

The curves are symmetrical about x/w = 0.5

Fig. 9 Transient concentration changes. Re = 590, z = 79.5 cm.

Ordinate: concentration difference bulk less interfacial ($M\ CuSO_4$)

Abscissa: square root of time after current switch-on ($min^{1/2}$)

——— Interfacial concentrations predicted by asymptotic solutions to the convective diffusion equation. Horizontal solid lines account for variation of diffusion coefficient D and cation transference number t_+ with electrolyte concentration,

— — — — ± 10% uncertainty in value of diffusion coefficient D_o

○ $i = 1.5\ mA/cm^2$
● $i = 3.0\ mA/cm^2$
interferometrically measured

Fig. 10 Transient concentration changes. Re = 1500.

○ $i = 5.0\ mA/cm^2$, $z = 5.0$ cm
● $i = 2.5\ mA/cm^2$, $z = 79.5$ cm

Other designations as in Figure 12.

Fig. 11 Derived current densities. Re = 590.

———— Level of applied current density

— — — — Represents ± 10% uncertainty in diffusion coefficient

● ▼ Derived by conventional analysis of the experimental interferograms eqs. 1 and 31.

0 ∇ Derived using a two-dimensional Pohlhausen-type boundary layer profile eq. 28.

0 ● $i = 1.5\ mA/cm^2$

∇ ▼ $i = 3.0\ mA/cm^2$

Fig. 12 Derived current densities. Re = 1500

0 ● $i = 2.5\ mA/cm^2$

∇ ▼ $i = 5.0\ mA/cm^2$

Other designations as in Fig. 11

Fig. 13 Derived laminar boundary layer thicknesses.

Ordinate: Nernst boundary layer thickness (mm)

Abscissa: Reduced distance from cathode leading page

———— Boundary layer thickness computed using eqs. 11 and 15.

— — — — represents ± 10% uncertainty in diffusion coefficient

○ $i = 1.5 mA/cm^2$ (Re = 590) or $i = 2.5 mA/cm^2$ (Re = 1500)

∇ $i = 3.0 mA/cm^2$ (Re = 590) or $i = 5.0 mA/cm^2$ (Re = 1500)

Fig. 14 Derived concentration changes for laminar flow, Re = 590.

Ordinate: Concentration change ΔC (M $CuSO_4$)

Abscissa: Reduced distance from cathode leading edge

———— ΔC computed using eqs. 11 and 15.

Other designations as in Fig. 13.

Fig. 15 Derived concentration changes for laminar flow, Re = 1500

Designations as in Fig. 14.

Fig. 16 Light curvature within the boundary layer.

▨	Electrode
░	Glass Sidewalls
ABC	deflected ray trajectory
DE	virtual plane of focus
FG	boundary layer edge

Other terms are defined in the Nomenclature

Fig. 17 Experimental interferograms of the interface between the electrode surface and homogeneous 0.1 M $CuSO_4$ electrolyte demonstrating the effect of electrode edge reflection.

A Location of real plane of focus (optically conjugate to the film plane of the camera) at x = -0.5 mm.

B at x = 0

C at x = 0.5 mm

D at x = 1.0 mm

Fig. 18 Interferogram analysis showing the effect of considering boundary layer variation across the channel.

Ordinate: distance y from electrode surface (mm)

Abscissa: electrolyte concentration (M $CuSO_4$) or phase change (fringes). The two abscissa scales are linearly related according to conventional interpretation of interferograms eqs. 1 and 31.

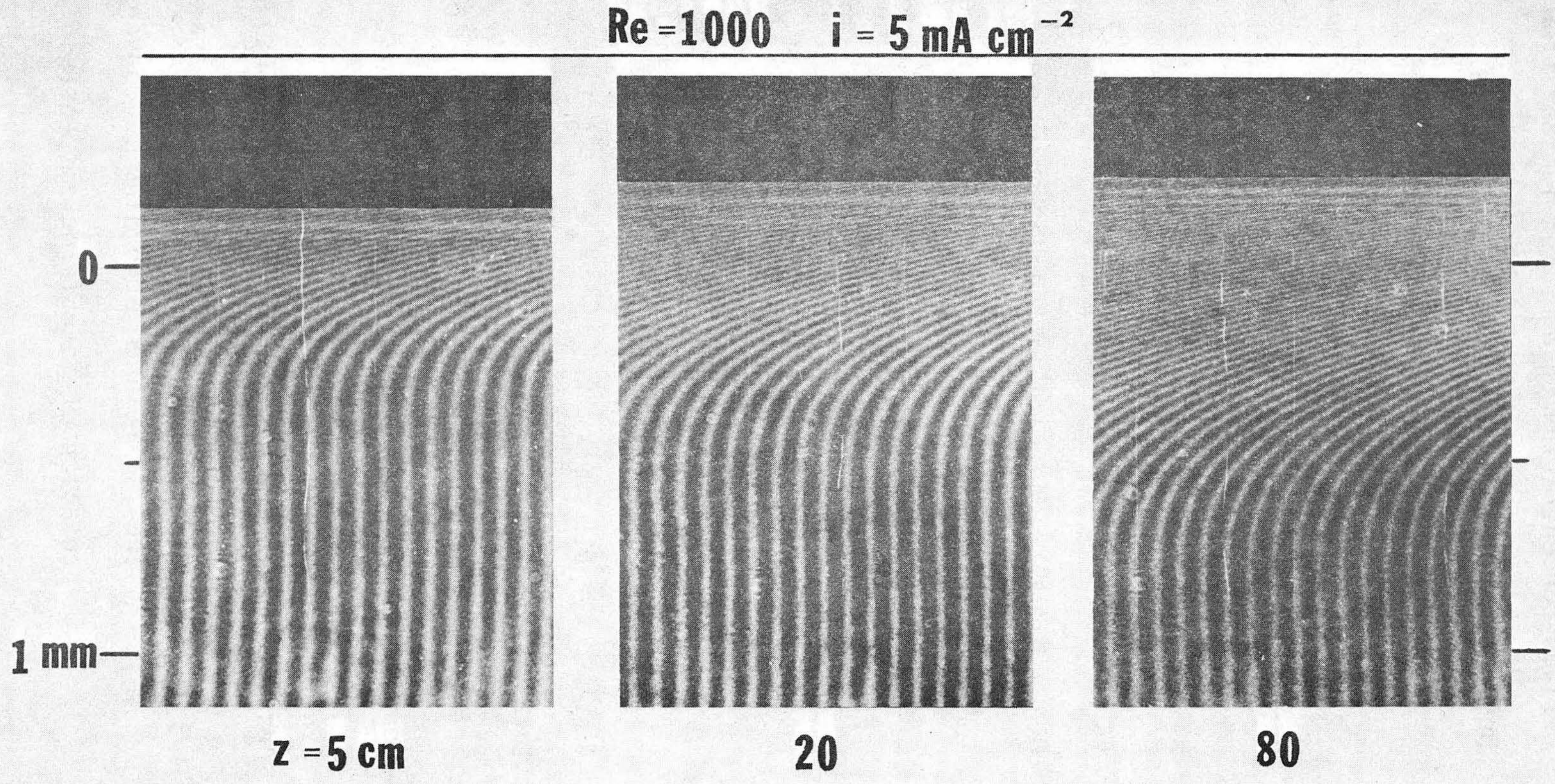

XBB 748-5797

Fig. 1

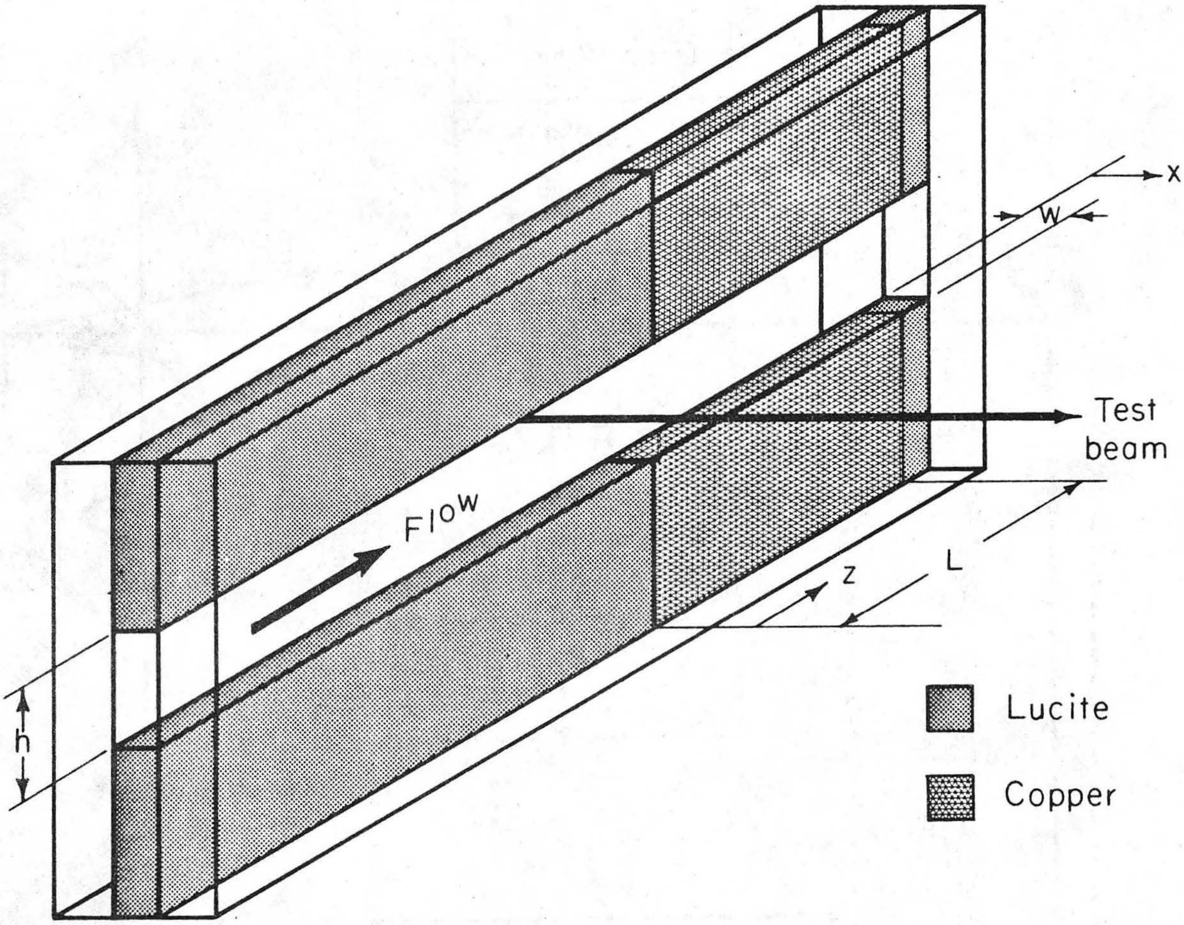

XBL 7410-4480

Fig. 2

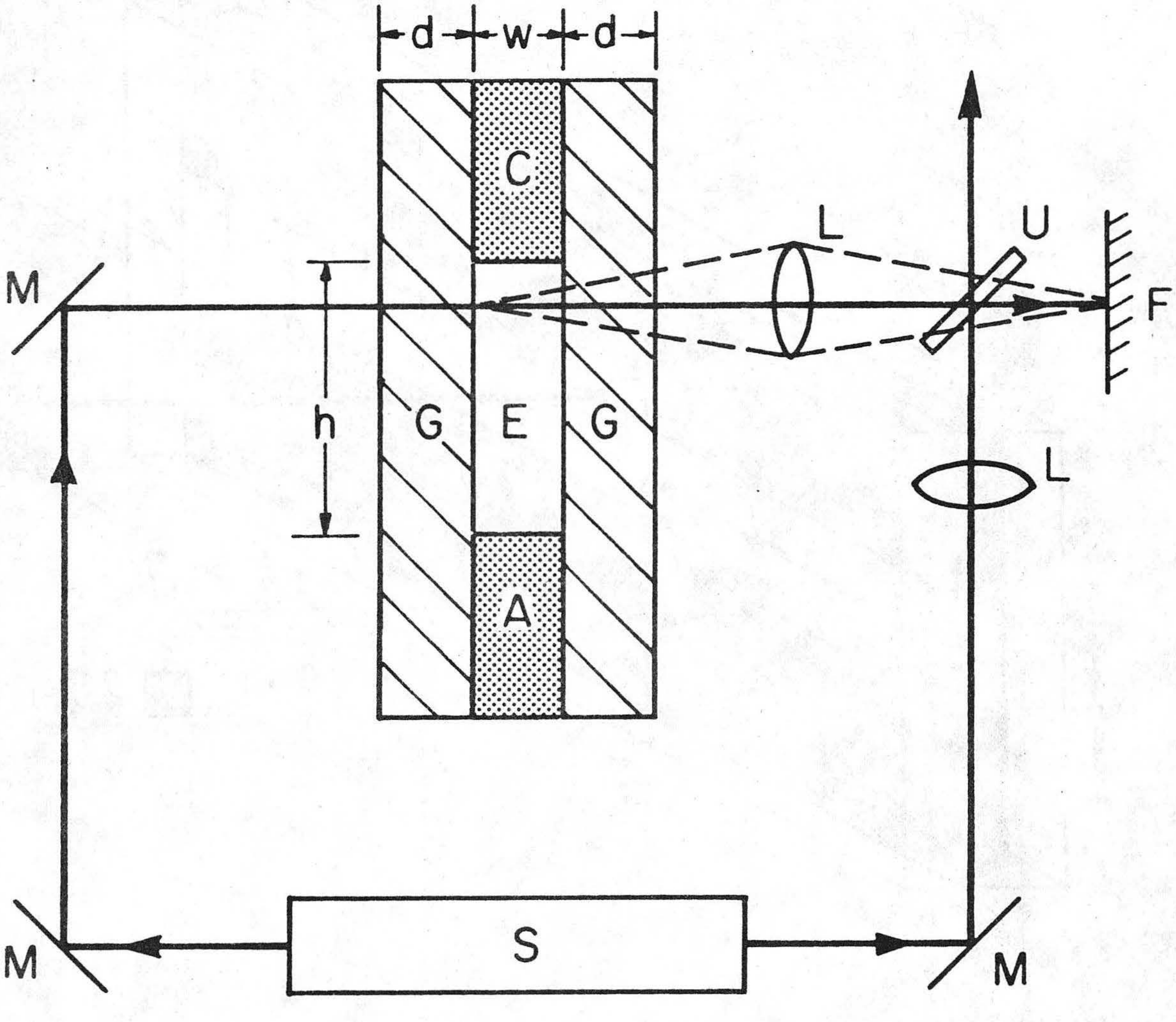

XBL749-4165

Fig. 3

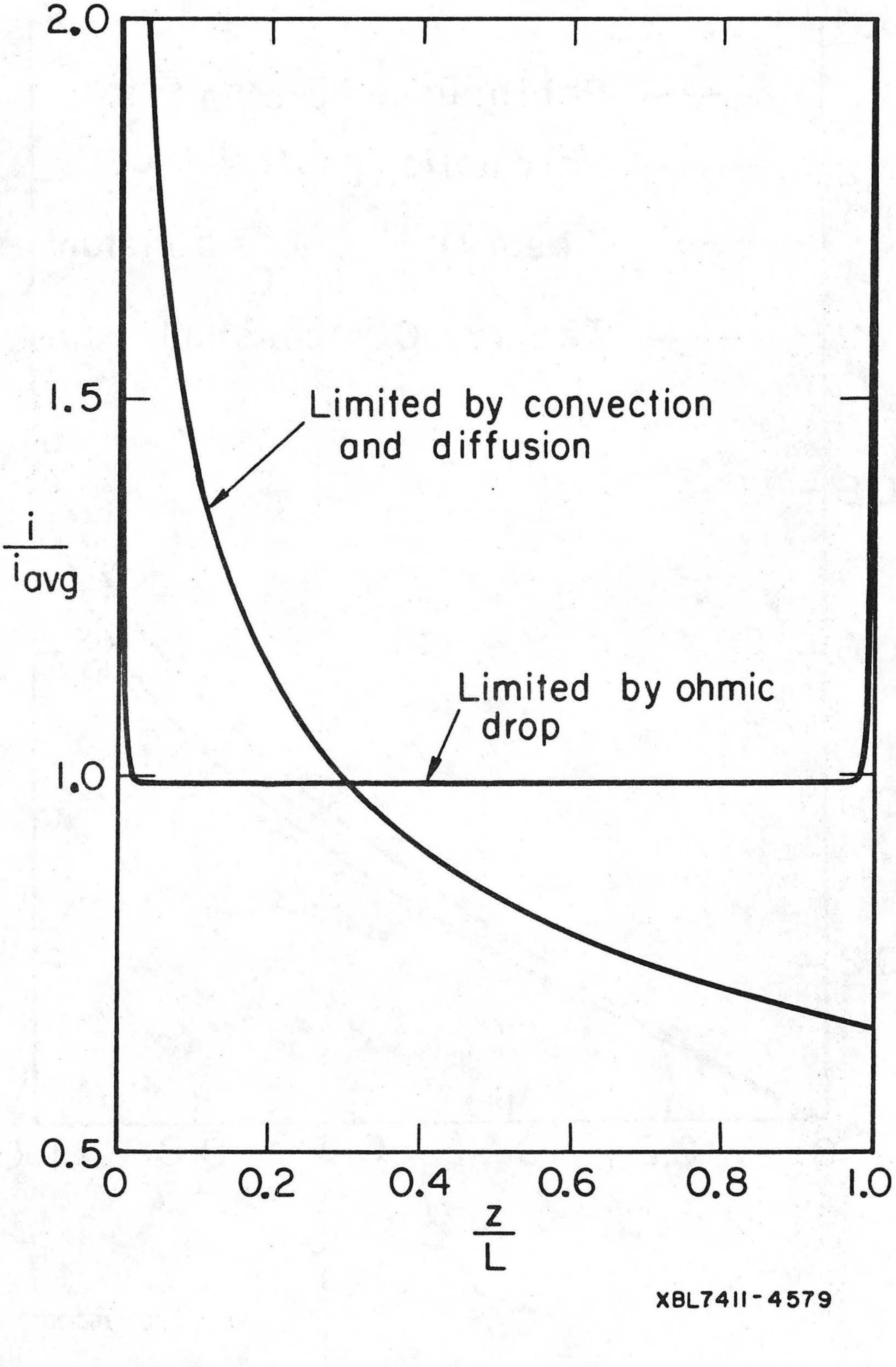
2.0
1.5
1.0
0.5
$\frac{i}{i_{avg}}$
0
0.2
0.4
0.6
0.8
1.0
$\frac{z}{L}$
Limited by convection and diffusion
Limited by ohmic drop
XBL7411-4579

Fig. 4

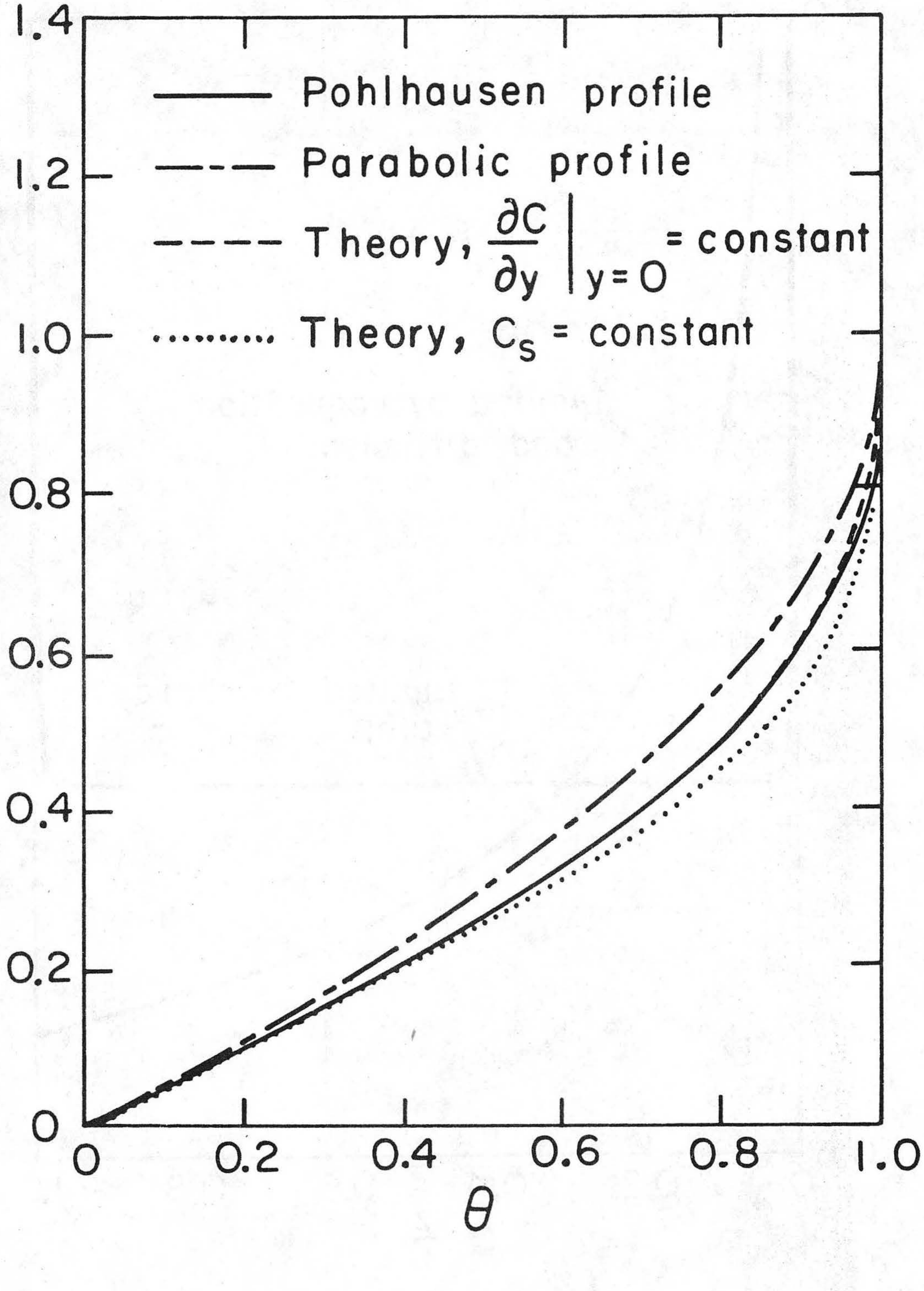

XBL 766-3012

Fig. 5

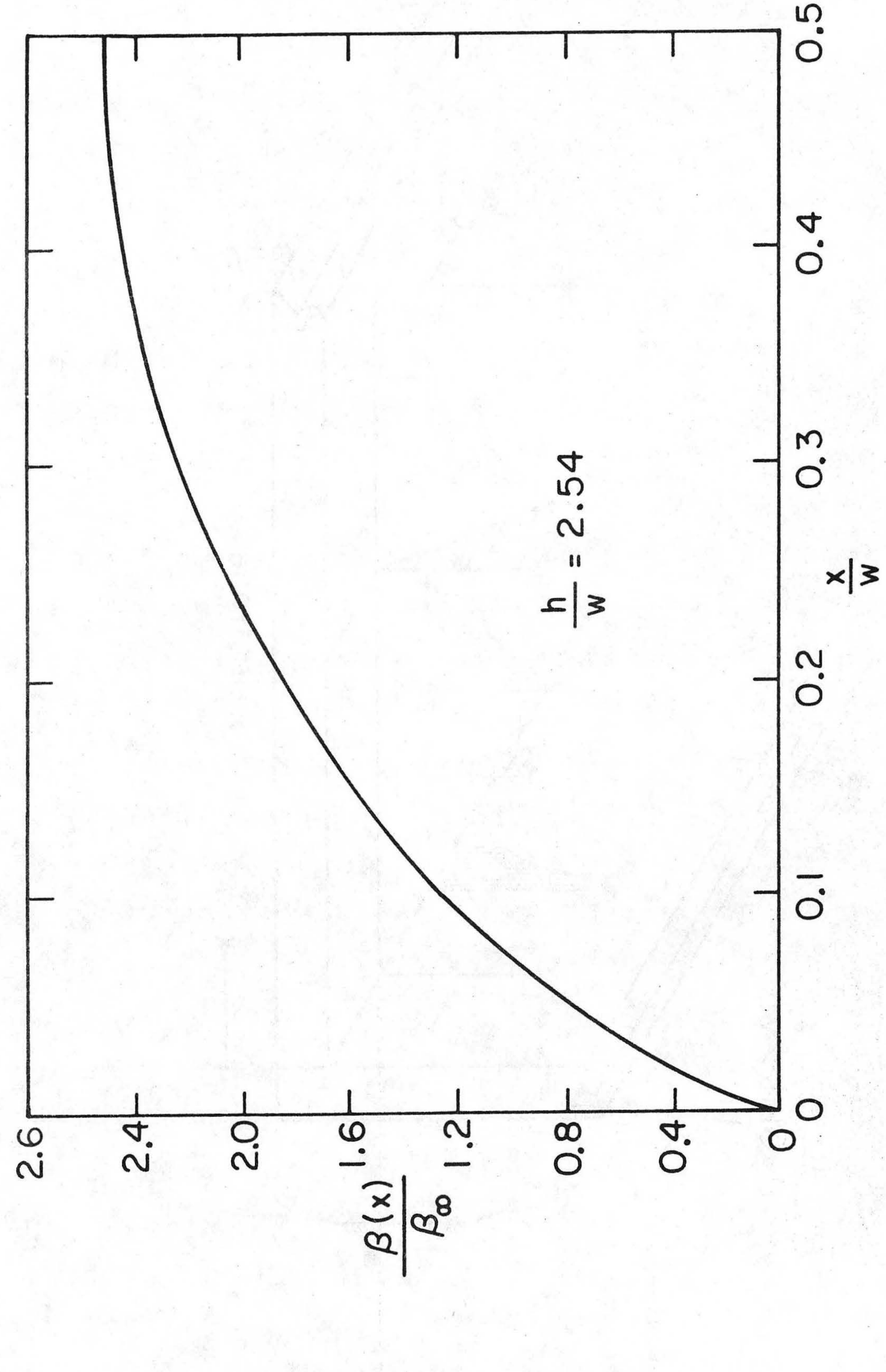

XBL 766-3011

Fig. 6

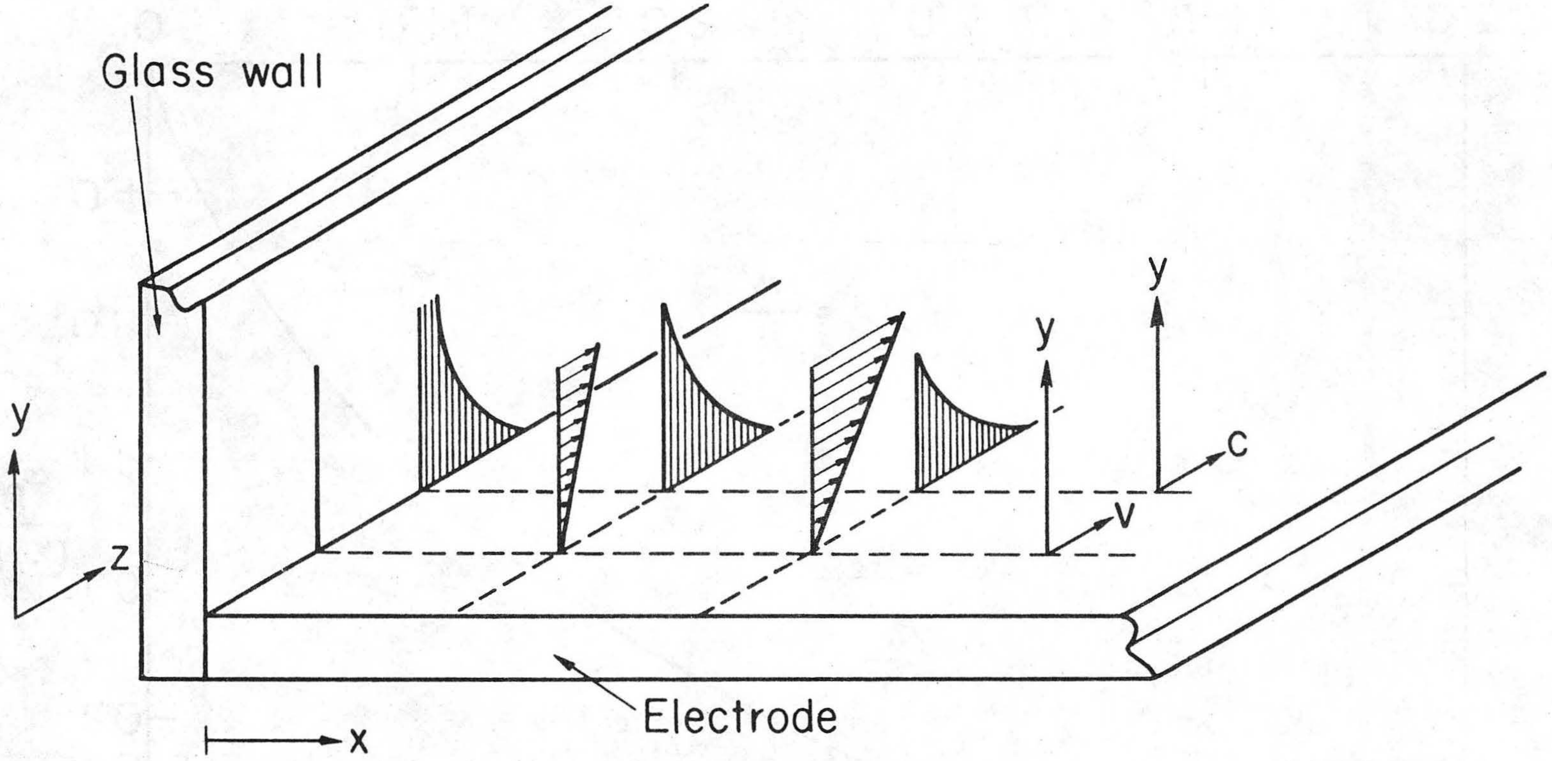

XBL775-3504

Fig. 7

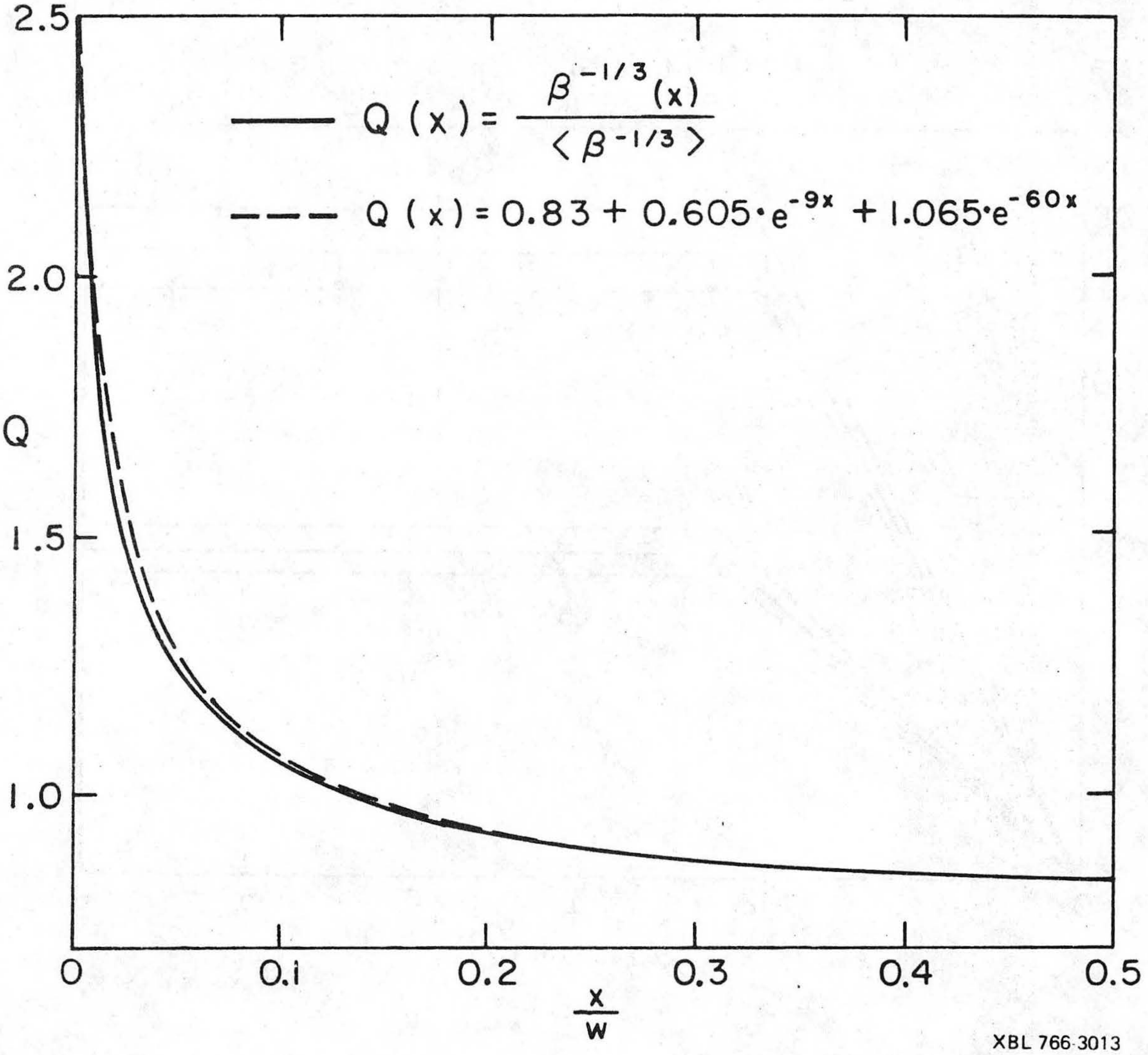
2.5
2.0
1.5
1.0
Q
$Q(x) = \frac{\beta^{-1/3}(x)}{\langle \beta^{-1/3} \rangle}$
$Q(x) = 0.83 + 0.605 \cdot e^{-9x} + 1.065 \cdot e^{-60x}$
0
0.1
0.2
0.3
0.4
0.5
$\frac{x}{w}$
XBL 766-3013

Fig. 8

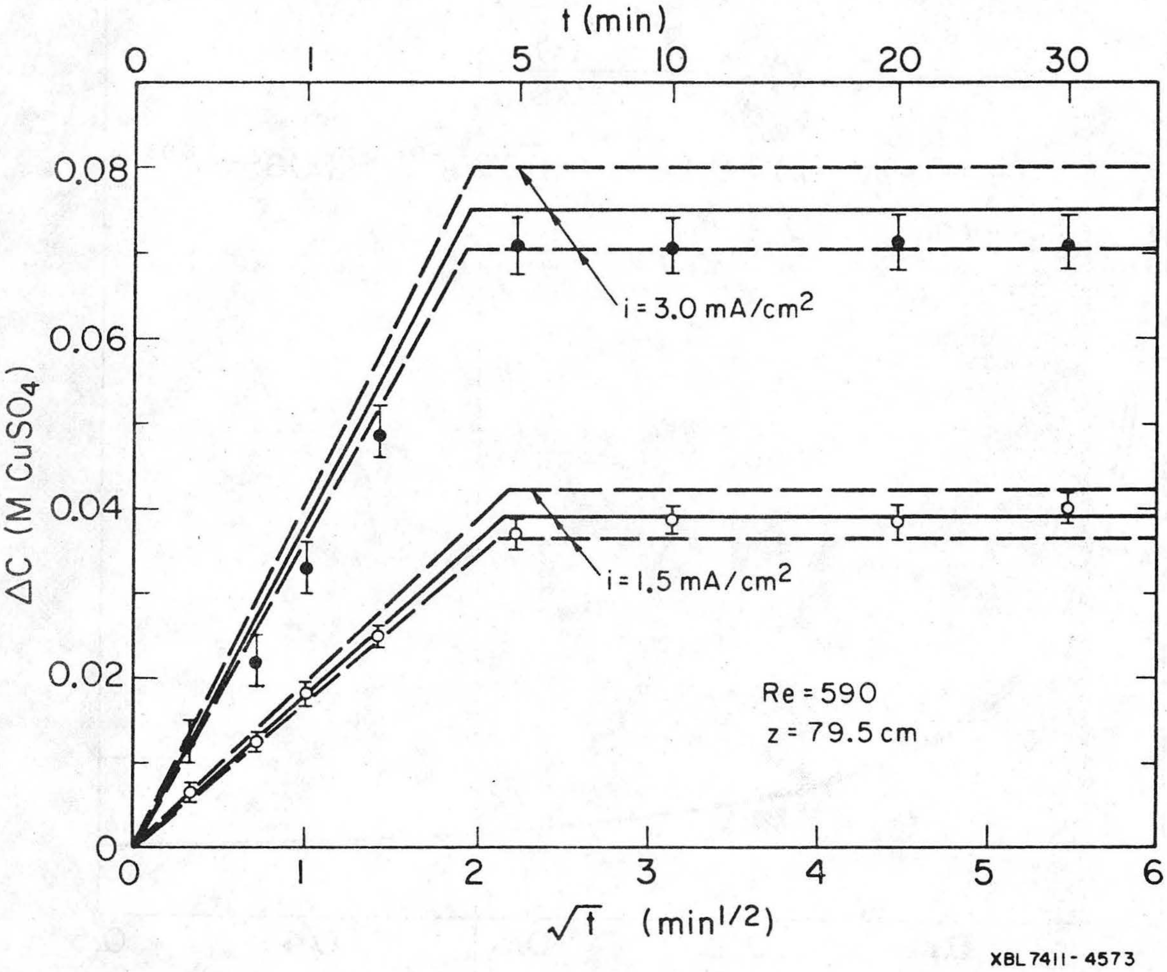
t (min)
0
1
5
10
20
30
0.08
0.06
0.04
0.02
0
ΔC (M CuSO4)
i = 3.0 mA/cm2
i = 1.5 mA/cm2
Re = 590
z = 79.5 cm
0
1
2
3
4
5
6
√t (min1/2)
XBL 7411-4573

Fig. 9

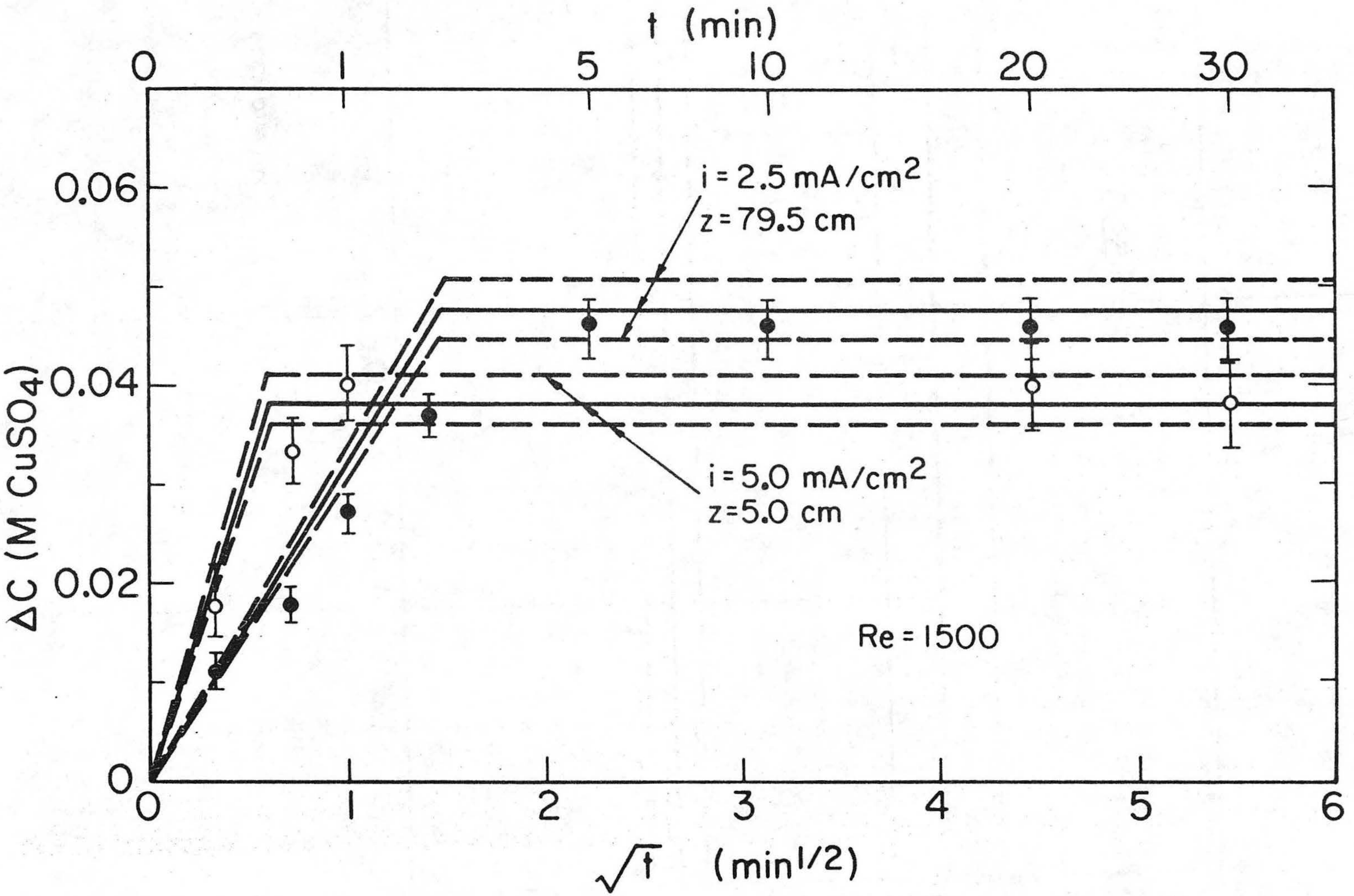

XBL 7411-4576

Fig. 10

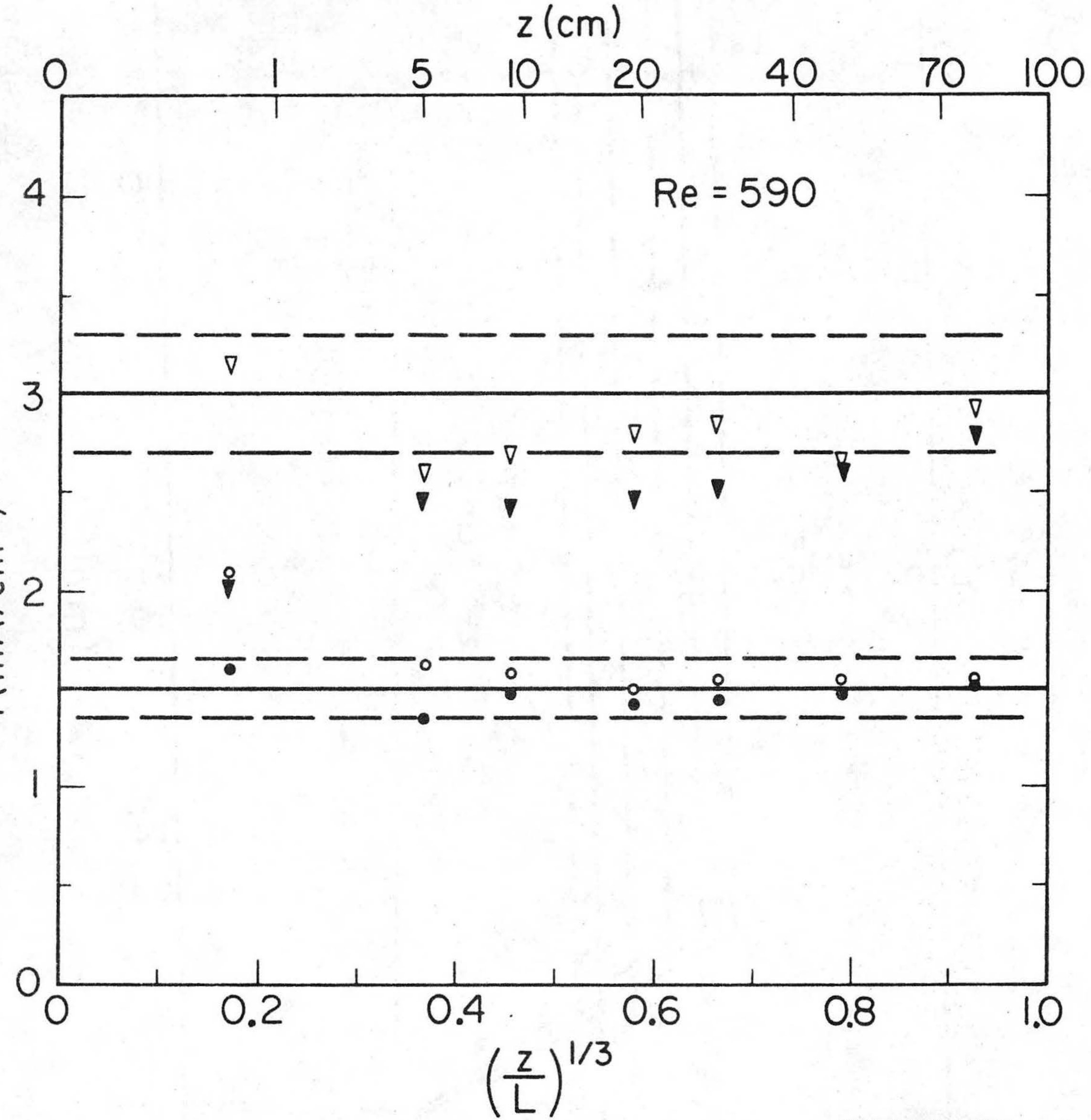

XBL7410-4376

Fig. 11

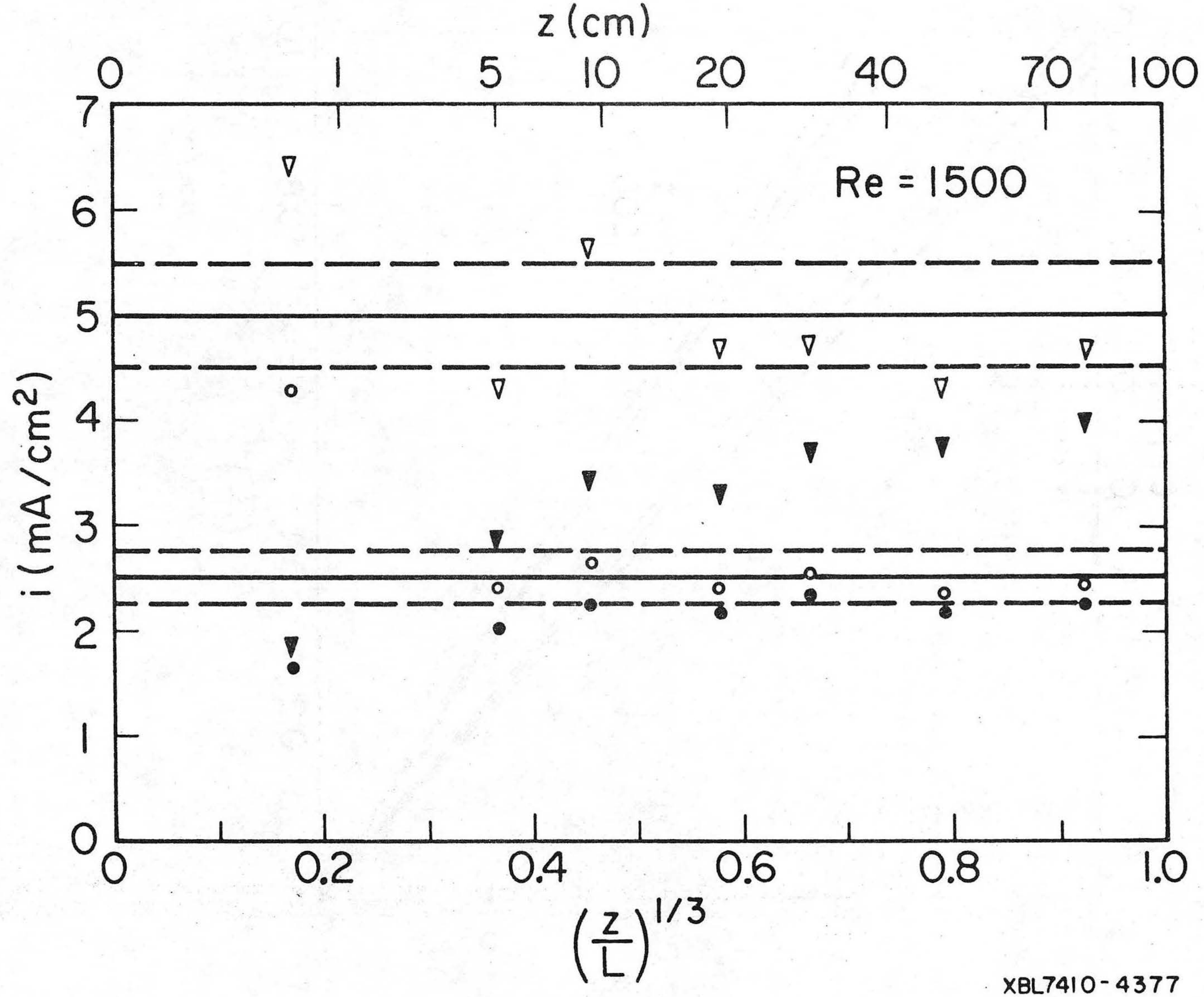

XBL7410-4377

Fig. 12

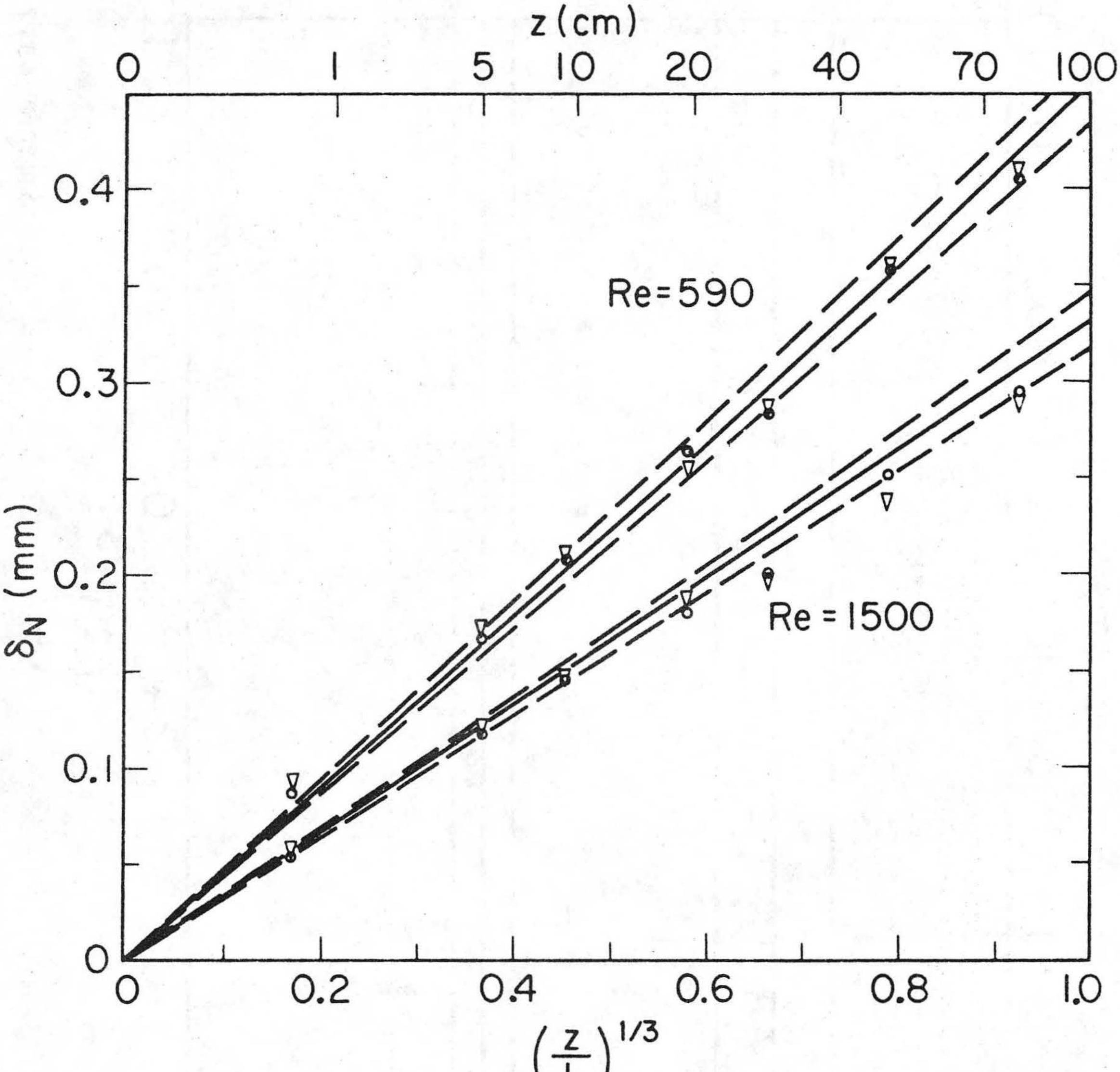

XBL7410-4374

Fig. 13

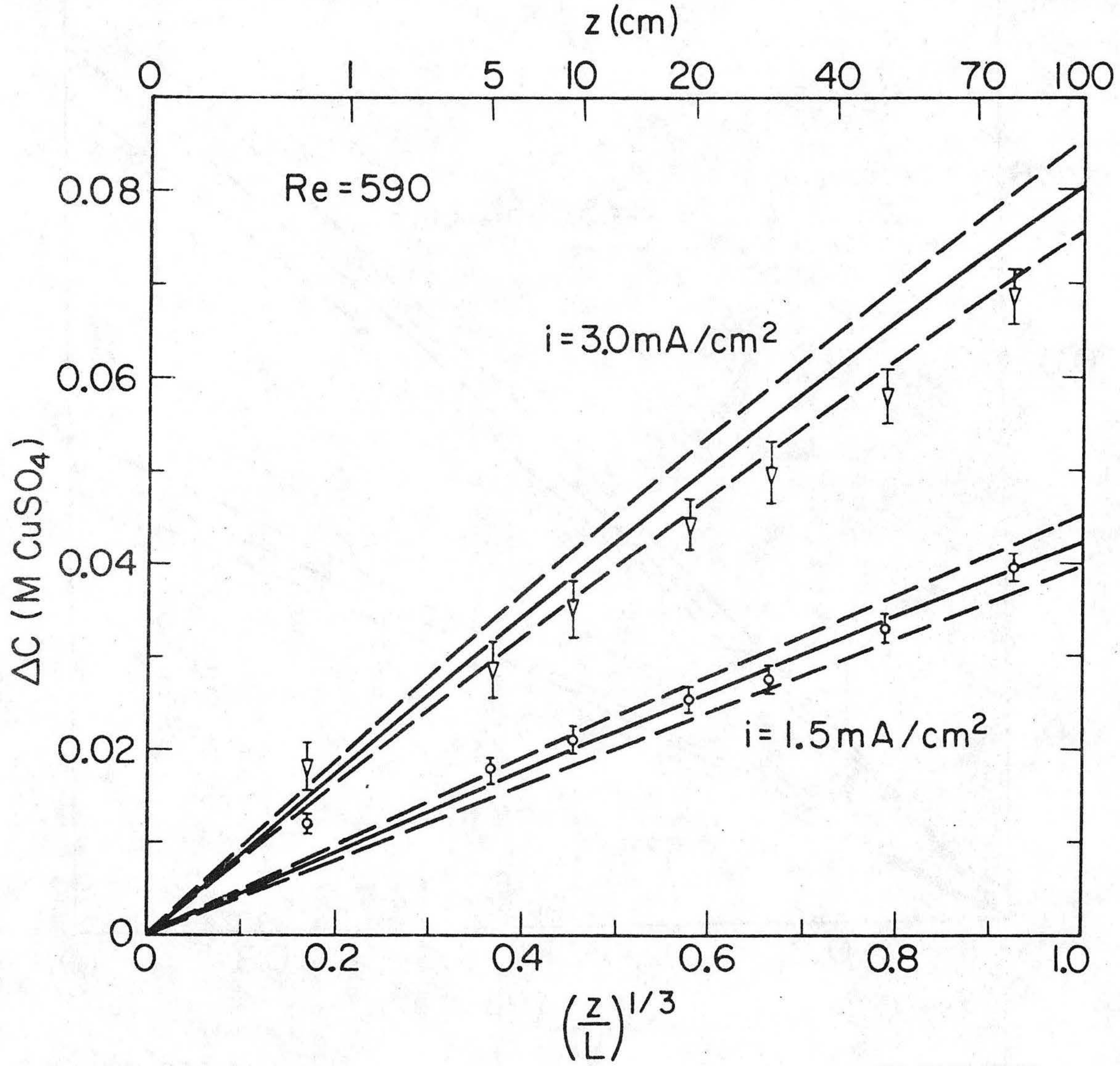

XBL 7410-4375

Fig. 14

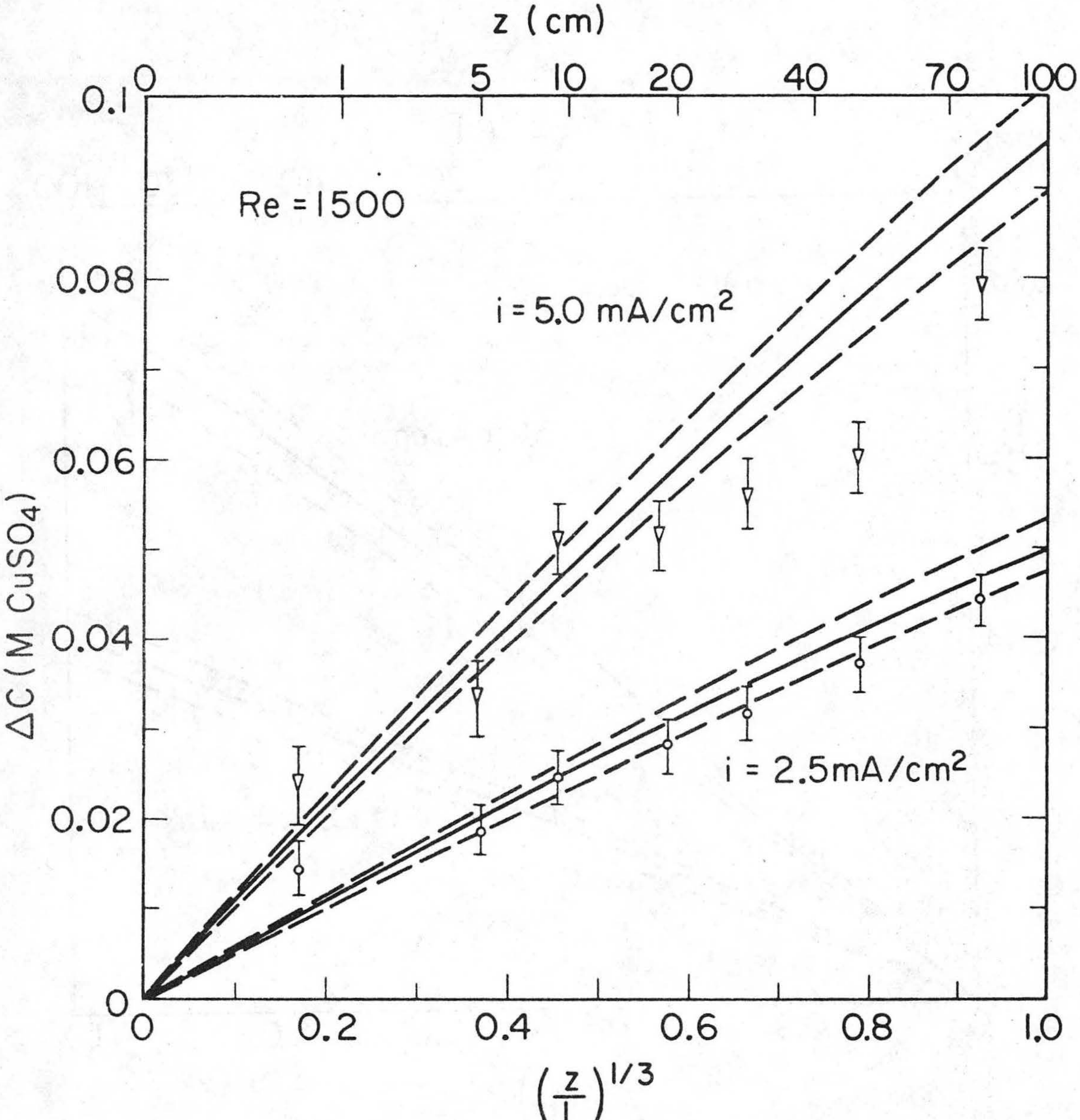

XBL7410-4373

Fig. 15

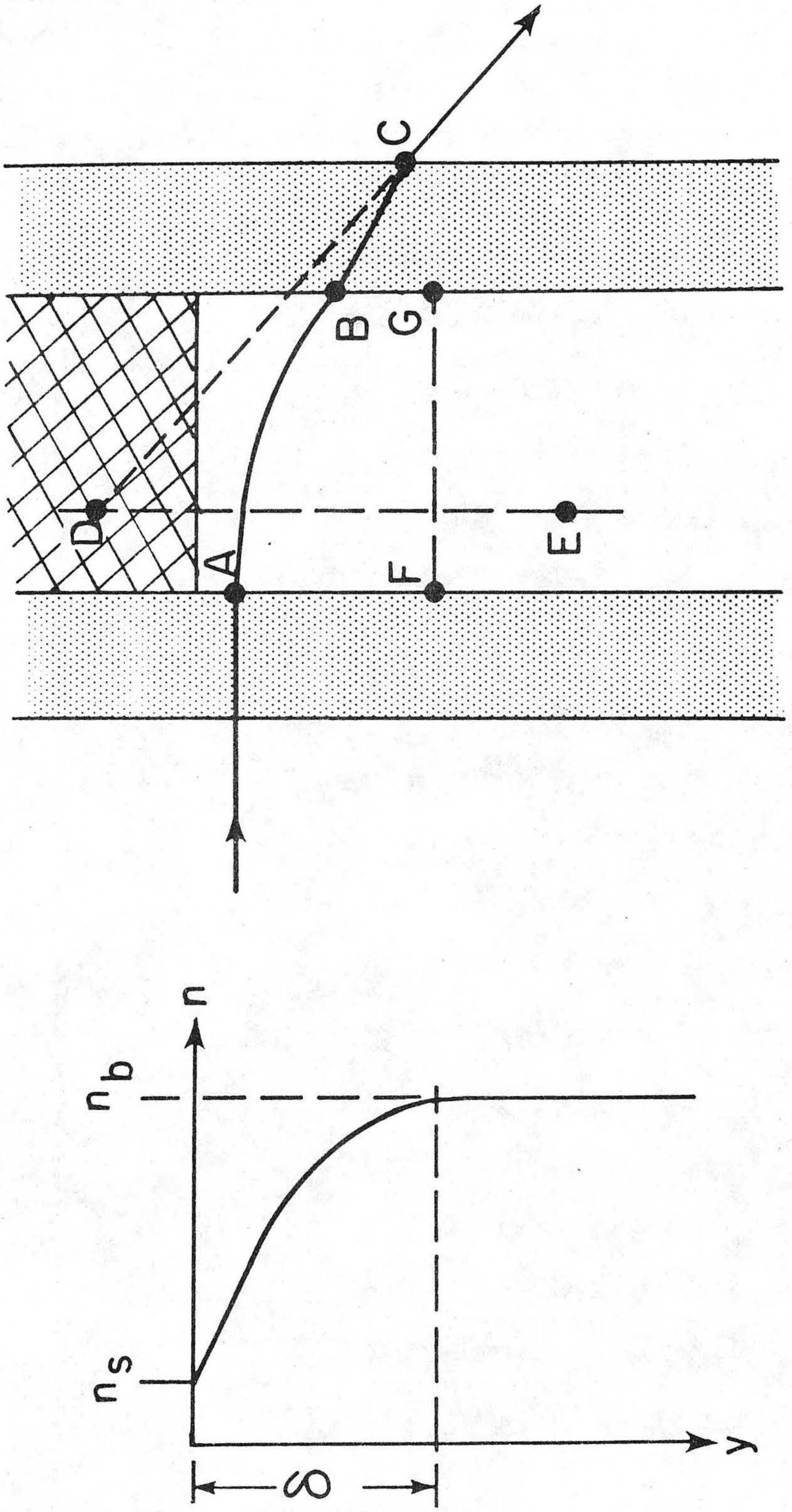

XBL 766-3014

Fig. 16

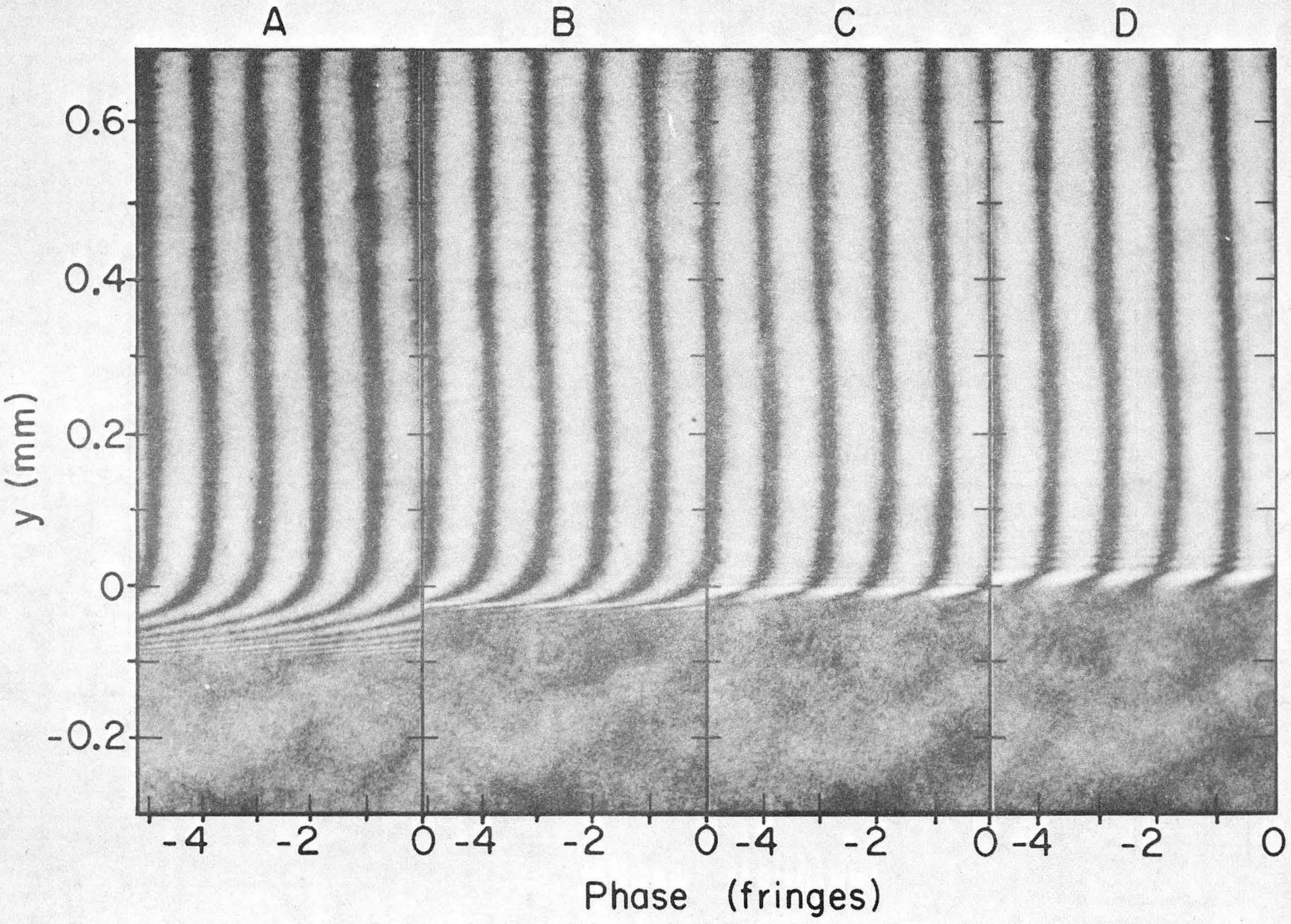

Fig. 17

XBB 7311-7012

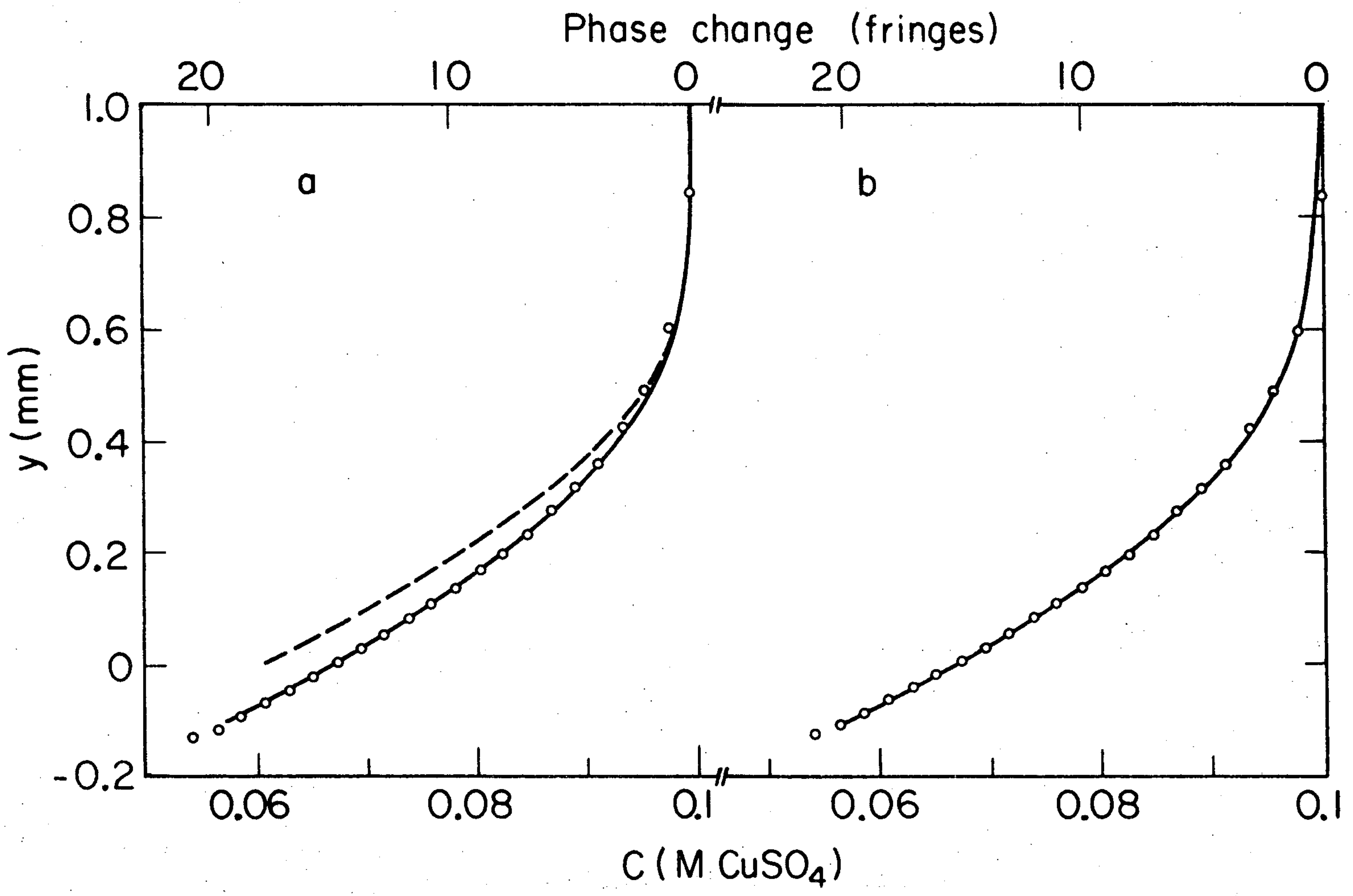

XBL7410-4381

Fig. 18

TECHNICAL INFORMATION DEPARTMENT
LAWRENCE BERKELEY LABORATORY
UNIVERSITY OF CALIFORNIA
BERKELEY, CALIFORNIA 94720